The Astrophysical Journal, 637:296–312, 2006 January 20

NUMERICAL 3+1 GENERAL RELATIVISTIC MAGNETOHYDRODYNAMICS: A LOCAL CHARACTERISTIC APPROACH

Luis Antón,[1] Olindo Zanotti,[1] Juan A. Miralles,[2] José M. Martí,[1]
José M. Ibáñez,[1] José A. Font,[1] and José A. Pons[2]
Received 2005 June 3; accepted 2005 September 20

ABSTRACT

We present a general procedure to solve numerically the general relativistic magnetohydrodynamics (GRMHD) equations within the framework of the 3+1 formalism. The work reported here extends our previous investigation in general relativistic hydrodynamics (Banyuls et al. 1997) where magnetic fields were not considered. The GRMHD equations are written in conservative form to exploit their hyperbolic character in the solution procedure. All theoretical ingredients necessary to build up high-resolution shock-capturing schemes based on the solution of local Riemann problems (i.e., Godunov-type schemes) are described. In particular, we use a renormalized set of regular eigenvectors of the flux Jacobians of the relativistic MHD equations. In addition, the paper describes a procedure based on the equivalence principle of general relativity that allows the use of Riemann solvers designed for special relativistic MHD in GRMHD. Our formulation and numerical methodology are assessed by performing various test simulations recently considered by different authors. These include magnetized shock tubes, spherical accretion onto a Schwarzschild black hole, equatorial accretion onto a Kerr black hole, and magnetized thick disks accreting onto a black hole and subject to the magnetorotational instability.

Subject headings: methods: numerical — MHD — relativity

1. INTRODUCTION

In several astrophysical scenarios both magnetic and gravitational fields play an important role in determining the evolution of the matter. In these scenarios it is a common fact that compact objects such as neutron stars are present, most of which have intense magnetic fields of order 10^{12}–10^{13} G, or even larger at birth, $\sim 10^{14}$–10^{15} G, as inferred from studies of anomalous X-ray pulsars and soft gamma-ray repeaters (Kouveliotou et al. 1998). In some cases, i.e., in the so-called magnetars, the magnetic fields can be so strong that they affect the internal structure of the star (Bocquet et al. 1995). In a different context, the most promising mechanisms for producing relativistic jets like those observed in active galactic nuclei and microquasars, as well as the ones conjectured to explain gamma-ray bursts, involve the hydromagnetic centrifugal acceleration of material from an accretion disk or the extraction of rotational energy from the ergosphere of a Kerr black hole (Penrose 1969; Blandford & Znajek 1977; Blandford & Payne 1982). In addition, the differential rotation of the magnetized plasma in the disk is responsible for the magnetorotational instability (MRI), which plays an important role in transporting angular momentum outward (Balbus & Hawley 1991).

If the gravitational field is strong enough, as in the vicinity of a compact object, the Newtonian description of gravity is only a rough approximation and general relativity becomes necessary. In such a theory, the so-called 3+1 formalism (Arnowitt et al. 1962) has proved particularly useful for numerical simulations involving time-dependent computations of hydrodynamical flows in curved spacetimes, either static or dynamic. The interested reader is referred to Font (2003) and references therein for an up-to-date overview of the different approaches that have been introduced during the years for solving the general relativistic hydrodynamics equations.

On the other hand, the inclusion of magnetic fields and the development of mathematical formulations of the magnetohydrodynamic (MHD) equations in a form suitable for efficient numerical implementations are still in an exploratory phase, although considerable progress has already been achieved in the last few years.

Numerical studies in special relativistic magnetohydrodynamics (SRMHD) have been undertaken by a growing number of authors (Komissarov 1999; Balsara 2001; Koldoba et al. 2002; Del Zanna et al. 2003; Leismann et al. 2005). In particular, Komissarov (1999), Balsara (2001), and Koldoba et al. (2002) developed independent *upwind* high-resolution shock-capturing (HRSC) schemes (also referred to as Godunov-type schemes), providing the characteristic information of the corresponding system of equations, which is the crucial building block in such types of schemes. In addition, Komissarov (1999) and Balsara (2001) proposed a comprehensive sample of tests to validate numerical MHD codes in special relativity (SR). Recently, Del Zanna et al. (2003) have developed a third-order shock-capturing *central* scheme for SRMHD that sidesteps the use of Riemann solvers in the solution procedure (for general definitions on HRSC schemes see, e.g., Toro 1997). Simulations of the morphology and dynamics of magnetized relativistic jets with Godunov-type schemes have been reported by Leismann et al. (2005). In addition, the exact solution of the Riemann problem in SRMHD, for some particular orientation of the magnetic field and the fluid velocity field, has been obtained by Romero et al. (2005) and extended by Giacomazzo & Rezzolla (2005) to general orientations.

Correspondingly, 3+1 representations of general relativistic MHD (GRMHD) were first analyzed by Sloan & Smarr (1985), Evans & Hawley (1988), Zhang (1989), Yokosawa (1993), and, more recently, by Koide et al. (1998), De Villiers & Hawley (2003a), Baumgarte & Shapiro (2003), Gammie et al. (2003),

[1] Departamento de Astronomía y Astrofísica, Universidad de Valencia, Edificio de Investigación, Dr. Moliner 50, 46100 Burjassot (Valencia), Spain.
[2] Departament de Física Aplicada, Universitat d'Alacant, Apartado Correus 99, 03080 Alacant, Spain.

Komissarov (2005), Duez et al. (2005), and Shibata & Sekiguchi (2005). Most of the existing applications to date are in the field of black hole accretion and jet formation. In Yokosawa (1993, 1995) the transport of energy and angular momentum in magnetohydrodynamical accretion onto a rotating black hole was studied adopting Wilson's formulation for the hydrodynamic equations (Wilson 1979), conveniently modified to account for the magnetic terms. The magnetic induction equation was solved using the constrained transport method of Evans & Hawley (1988). Later on, Koide and coworkers performed the first MHD simulations of jet formation in general relativity (Koide et al. 1998, 2000) in the context of the Blandford-Payne mechanism. These authors solved the MHD equations in the test fluid approximation (in the background geometry of Schwarzschild/Kerr spacetimes) using a second-order finite-difference central scheme with nonlinear dissipation. Employing the same numerical approach, Koide et al. (2002) and Koide (2003) studied the validity of the so-called MHD Penrose process to extract rotational energy from a Kerr black hole by simulating the evolution of a rarefied plasma with a uniform magnetic field. Komissarov (2005) has also recently investigated this topic, finding evidence in favor of the extraction of rotational energy of the black hole by the Blandford-Znajek mechanism (Blandford & Znajek 1977) but against the development of strong relativistic outflows or jets. The long-term solution found by Komissarov (2005) shows properties that are significantly different from those of the short initial (transient) phase studied by Koide (2003). An additional astrophysical application in the context of electromagnetic extraction of energy from a Kerr black hole is represented by the analysis of McKinney & Gammie (2004), who have compared the analytic prediction of Blandford & Znajek (1977) with time evolution calculations. Finally, two different groups (De Villiers & Hawley 2003a, 2003b; Gammie et al. 2003) have started programs to investigate the time-varying behavior of magnetized accretion flows onto Kerr black holes, with great emphasis on the issue of the development of the MRI in thick accretion disks (see also Yokosawa & Inui 2005). While De Villiers & Hawley (2003a, 2003b) adopt a nonconservative (ZEUS like) scheme, the approach followed by Gammie et al. (2003) is based on a conservative HRSC scheme, namely, the so-called HLL scheme of Harten et al. (1983).

In light of the existing literature on the subject, it is clear that astrophysical applications of Godunov-type schemes in GRMHD have been reported only very recently (Gammie et al. 2003; Komissarov 2005; Duez et al. 2005). Our goal in this paper is to present the evolution equations for the magnetic field and for the fluid within the 3+1 formalism, formulated in a suitable way to apply Godunov-type schemes based on (approximate) Riemann solvers. Our numerical procedure uses two original ingredients. On the one hand, the code incorporates a local coordinate transformation to Minkowskian coordinates, similar to the one developed for relativistic hydrodynamics in Pons et al. (1998), prior to the computation of the numerical fluxes. In this way, Riemann solvers designed for SRMHD can be straightforwardly used in GRMHD calculations. We note that Komissarov (2005) applies the same approach, using an HRSC scheme based on the SR Riemann solver described in Komissarov (1999) and adapted to general relativity following the procedure laid out in Pons et al. (1998). We present here, however, a number of tests assessing the feasibility of the approach. As a second novel ingredient, we use a *renormalized* set of right and left eigenvectors of the flux vector Jacobians of the SRMHD equations that are regular and span a complete basis in any physical state, including degenerate states.

The organization of the paper is as follows. We start by introducing the mathematical framework in § 2, including the essentials of the 3+1 formalism, the description of the magnetic field, the induction equation and the conservation equations of particle number, and the stress-energy tensor in conservative form. A brief analysis of the hyperbolic structure of the GRMHD system of equations is given in § 3. The numerical procedure to solve the equations is described in § 4. Finally, in § 5 we present the results of some numerical tests and applications in order to assess our formulation and methodology. The summary of our work is given in § 6. Throughout the paper Latin indices run from 1 to 3 and Greek indices from 0 to 3. Four-vectors are indistinctly denoted using index notation or boldface letters, e.g., u^μ, $\boldsymbol{u}$. We adopt geometrized units by setting $c = G = 1$.

2. MATHEMATICAL FRAMEWORK

2.1. *The Eulerian Observer in the* 3+1 *Formalism*

In the 3+1 formalism the line element of the spacetime can be written as

$$ds^2 = -\left(\alpha^2 - \beta_i\beta^i\right) dt^2 + 2\beta_i\, dx^i\, dt + \gamma_{ij}\, dx^i\, dx^j, \quad (1)$$

where α (lapse function), β^i (shift vector), and γ_{ij} (spatial metric) are functions of the coordinates t, x^i. A natural observer associated with the 3+1 splitting is the one with four-velocity $\boldsymbol{n}$ perpendicular to the hypersurfaces of constant t at each event in the spacetime. This is the so-called Eulerian observer.[3] The contravariant and covariant components of $\boldsymbol{n}$ are given by

$$n^\mu = \frac{1}{\alpha}\left(1,\ -\beta^i\right) \quad (2)$$

and

$$n_\mu = (-\alpha,\ 0,\ 0,\ 0), \quad (3)$$

respectively. In spacetimes containing matter an additional natural observer is the one that follows the fluid during its motion, also called the "comoving observer," with four-velocity $\boldsymbol{u}$. With the standard definition, the three-velocity of the fluid as measured by the Eulerian observer can be expressed as

$$v^i \equiv \frac{h^i_\mu u^\mu}{-\boldsymbol{u}\cdot\boldsymbol{n}}, \quad (4)$$

where $-\boldsymbol{u}\cdot\boldsymbol{n} \equiv W$ is the relative Lorentz factor between $\boldsymbol{u}$ and $\boldsymbol{n}$, while $h_{\mu\nu} = g_{\mu\nu} + n_\mu n_\nu$ is the projector onto the hypersurface orthogonal to $\boldsymbol{n}$, whose spatial terms are given by $h_{ij} = \gamma_{ij}$. From equation (4) it follows that

$$v^i = \frac{u^i}{\alpha u^t} + \frac{\beta^i}{\alpha}, \quad (5)$$

while $v_i = u_i/W$. Note that the Lorentz factor satisfies the relation $W = 1/(1 - v^2)^{1/2} = \alpha u^t$, where $v^2 = \gamma_{ij} v^i v^j$ is the squared modulus of the three-velocity of the fluid with respect to the Eulerian observer.

2.2. *Magnetic Field Evolution*

A complete description of the electromagnetic field in general relativity is provided by the Faraday electromagnetic tensor field $F^{\mu\nu}$. This tensor is related to the electric and magnetic field, E^μ

[3] In the Kerr metric this Eulerian observer is indeed the observer with zero azimuthal angular momentum (ZAMO) as measured from infinity.

and B^μ, measured by a generic observer with four-velocity U^μ, as follows:

$$F^{\mu\nu} = U^\mu E^\nu - U^\nu E^\mu - \eta^{\mu\nu\lambda\delta} U_\lambda B_\delta, \tag{6}$$

$\eta^{\mu\nu\lambda\delta}$ being the volume element,

$$\eta^{\mu\nu\lambda\delta} = \frac{1}{\sqrt{-g}}[\mu\nu\lambda\delta], \tag{7}$$

where g is the determinant of the four-metric ($g = \det g_{\mu\nu}$) and $[\mu\nu\lambda\delta]$ is the completely antisymmetric Levi-Civita symbol. Both $\boldsymbol{E}$ and $\boldsymbol{B}$ are orthogonal to $\boldsymbol{U}$, $\boldsymbol{E}\cdot\boldsymbol{U} = \boldsymbol{B}\cdot\boldsymbol{U} = 0$. The dual of the electromagnetic tensor ${}^*F^{\mu\nu}$ is defined as

$${}^*F^{\mu\nu} = \tfrac{1}{2}\eta^{\mu\nu\lambda\delta} F_{\lambda\delta}, \tag{8}$$

and in terms of the electric and magnetic field measured by the observer $\boldsymbol{U}$ is given by

$${}^*F^{\mu\nu} = U^\mu B^\nu - U^\nu B^\mu + \eta^{\mu\nu\lambda\delta} U_\lambda E_\delta. \tag{9}$$

From these equations, $\boldsymbol{E}$ and $\boldsymbol{B}$ can be expressed in terms of the electromagnetic tensor and the four-velocity $\boldsymbol{U}$ as follows:

$$E^\mu = F^{\mu\nu} U_\nu, \tag{10}$$

$$B^\mu = {}^*F^{\mu\nu} U_\nu. \tag{11}$$

In terms of the electromagnetic tensor, Maxwell's equations are written as follows:

$$\nabla_\nu {}^*F^{\mu\nu} = 0, \tag{12}$$

$$\nabla_\nu F^{\mu\nu} = 4\pi \mathcal{J}^\mu, \tag{13}$$

where ∇_ν stands for the covariant derivative and $\mathcal{J}^\mu$ is the electric four-current. According to Ohm's law, the latter can be in general expressed as

$$\mathcal{J}^\mu = \rho_q u^\mu + \sigma F^{\mu\nu} u_\nu, \tag{14}$$

where ρ_q is the proper charge density measured by the comoving observer and σ is the electric conductivity. Maxwell's equations can be further simplified if one assumes that the fluid is a perfect conductor. In this case the fluid has infinite conductivity and, in order to keep the current finite, the term proportional to the conduction current, $F^{\mu\nu}u_\nu$, must vanish, which means that the electric field measured by the comoving observer is zero. This case corresponds to the so-called ideal MHD condition. We can take advantage of this condition to express the electric field measured by the observer $\boldsymbol{U}$ as a function of the magnetic field $\boldsymbol{B}$ measured by the same observer and of the four-velocities U^μ and u^μ. Straightforward calculations give

$$E^\mu = \frac{1}{W}\eta^{\mu\nu\lambda\delta} u_\nu U_\lambda B_\delta. \tag{15}$$

If we choose $\boldsymbol{U}$ as the four-velocity of the Eulerian observer, $\boldsymbol{U} = \boldsymbol{n}$, equation (15) provides

$$E^0 = 0, \tag{16}$$

$$E^i = -\alpha\eta^{0ijk} v_j B_k, \tag{17}$$

or, in terms of three-vectors, $\vec{E} = -\vec{v}\times\vec{B}$, where the arrow means that the vector lies in the "absolute space" and the cross product is defined using the induced volume element in the absolute space $\eta^{ijk} = \alpha\eta^{0ijk}$. Using the above relations, the dual of the electromagnetic field can be written in terms of the magnetic field only,

$${}^*F^{\mu\nu} = \frac{u^\mu B^\nu - u^\nu B^\mu}{W}, \tag{18}$$

and Maxwell's equations $\nabla^*_\nu F^{\mu\nu} = 0$ reduce to the divergence-free condition plus the induction equation for the evolution of the magnetic field,

$$\frac{\partial(\sqrt{\gamma}B^i)}{\partial x^i} = 0, \tag{19}$$

$$\frac{1}{\sqrt{\gamma}}\frac{\partial}{\partial t}(\sqrt{\gamma}B^i) = \frac{1}{\sqrt{\gamma}}\frac{\partial}{\partial x^j}\Big\{\sqrt{\gamma}\Big[(\alpha v^i - \beta^i)B^j - (\alpha v^j - \beta^j)B^i\Big]\Big\}, \tag{20}$$

or, in terms of three-vectors,

$$\vec{\nabla}\cdot\vec{B} = 0, \tag{21}$$

$$\frac{1}{\sqrt{\gamma}}\frac{\partial}{\partial t}\left(\sqrt{\gamma}\vec{B}\right) = \vec{\nabla}\times\left[\left(\alpha\vec{v} - \vec{\beta}\right)\times\vec{B}\right]. \tag{22}$$

2.3. *Conservation Equations*

Once we have established the magnetic field evolution equation in the ideal MHD case, we need to obtain the evolution equations for the matter fields. These equations can be expressed as the local conservation laws of baryon number and energy momentum. For the baryon number we have

$$\nabla_\nu J^\nu = 0, \tag{23}$$

$\boldsymbol{J}$ being the rest-mass current, $J^\mu = \rho u^\mu$, where ρ denotes the rest-mass density. The conservation of the energy momentum is given by

$$\nabla_\nu T^{\mu\nu} = 0, \tag{24}$$

where $T^{\mu\nu}$ is the energy-momentum tensor. For a fluid endowed with a magnetic field, this tensor is obtained by adding the energy-momentum tensor of the fluid to that of the electromagnetic field:

$$T^{\mu\nu} = T^{\mu\nu}_{\rm fluid} + T^{\mu\nu}_{\rm EM}. \tag{25}$$

When the fluid is assumed to be perfect, $T^{\mu\nu}_{\rm fluid}$ is given by

$$T^{\mu\nu}_{\rm fluid} = \rho h u^\mu u^\nu + p g^{\mu\nu}, \tag{26}$$

where $g_{\mu\nu}$ is the metric, p is the pressure, and h is the specific enthalpy, defined by $h = 1 + \varepsilon + p/\rho$, ε being the specific internal energy. The fluid is further assumed to be in local thermodynamic equilibrium, and there exists an equation of state of the form $p = p(\rho,\ \varepsilon)$ that relates the pressure with ρ and ε. On the other hand, the energy-momentum tensor $T^{\mu\nu}_{\rm EM}$ of the electromagnetic field can be obtained from the electromagnetic tensor, $\boldsymbol{F}$, as follows:

$$T^{\mu\nu}_{\rm EM} = \frac{1}{4\pi}\left(F^{\mu\lambda}F^\nu_\lambda - \frac{1}{4}g^{\mu\nu}F^{\lambda\delta}F_{\lambda\delta}\right). \tag{27}$$

Furthermore, from equation (6) and exploiting the ideal MHD condition, the electromagnetic tensor can be expressed in terms of the magnetic field b^μ measured by the comoving observer as

$$F^{\mu\nu} = -\eta^{\mu\nu\lambda\delta} u_\lambda b_\delta, \tag{28}$$

and equation (27) can be rewritten as

$$T^{\mu\nu}_{\rm EM} = \left(u^\mu u^\nu + \tfrac{1}{2} g^{\mu\nu}\right) b^2 - b^\mu b^\nu, \tag{29}$$

where $b^2 = b^\nu b_\nu$ and where the magnetic field four-vector has been redefined by dividing it by the factor $(4\pi)^{1/2}$. As a result, the total energy-momentum tensor, fluid plus electromagnetic field, is given by

$$T^{\mu\nu} = \rho h^* u^\mu u^\nu + p^* g^{\mu\nu} - b^\mu b^\nu, \tag{30}$$

where we have introduced the definitions $p^* = p + b^2/2$ and $h^* = h + b^2/\rho$. Note that if we consistently define $\varepsilon^* = \varepsilon + b^2/(2\rho)$, the relation $h^* = 1 + \varepsilon^* + p^*/\rho$ is fulfilled.

In order to write the evolution equations (23) and (24) in a conservation form suitable for numerical applications, let us define a basis adapted to the Eulerian observer,

$$\boldsymbol{e}_{(\lambda)} = \{\boldsymbol{n},\ \partial_i\}, \tag{31}$$

where ∂_i are the coordinate vectors that are tangent to the hypersurface $t = \text{const}$ and, therefore, $\boldsymbol{n} \cdot \partial_i = 0$. This allows us to define the following five four-vectors $\mathcal{D}_{(A)}$:

$$\mathcal{D}_{(A)} = \left\{\boldsymbol{T}\left(\boldsymbol{e}_{(\lambda)}, \cdot\right), \boldsymbol{J}\right\}, \quad A = 0, \ldots, 4. \tag{32}$$

Hence, the above system of equations (23) and (24) can be written as

$$\nabla_\nu \mathcal{D}^\nu_{(A)} = s_{(A)}, \tag{33}$$

where the five quantities $s_{(A)}$ on the right-hand side—*the sources*—are

$$s_{(A)} = \left\{T^{\alpha\beta}\nabla_\mu e_{(\lambda)\nu},\ 0\right\}. \tag{34}$$

The covariant derivatives of the basis vectors, $\nabla_\mu e_{(\lambda)\nu}$, are obtained in the usual manner as

$$\nabla_\mu e_{(\lambda)\nu} = \frac{\partial e_{(\lambda)\nu}}{\partial x^\mu} - \Gamma^\delta_{\nu\mu} e_{(\lambda)\delta}, \tag{35}$$

where $\Gamma^\delta_{\nu\mu}$ are the Christoffel symbols and

$$e_{(0)\nu} = -\alpha\delta_{0\nu}, \quad e_{(k)\nu} = g_{k\nu} = \left(\beta_k,\ \gamma_{kj}\right). \tag{36}$$

In a similar way to the pure hydrodynamics case (Banyuls et al. 1997), if we now define the following quantities measured by an Eulerian observer,

$$D \equiv -J_\nu n^\nu = \rho W, \tag{37}$$

$$S_j \equiv -\boldsymbol{T}\left(\boldsymbol{n},\ \boldsymbol{e}_{(j)}\right) = \rho h^* W^2 v_j - \alpha b^0 b_j, \tag{38}$$

$$\tau \equiv \boldsymbol{T}(\boldsymbol{n},\ \boldsymbol{n}) = \rho h^* W^2 - p^* - \alpha^2 \left(b^0\right)^2 - D, \tag{39}$$

i.e., the rest-mass density, the momentum density of the magnetized fluid in the j-direction, and its total energy density (subtracting the rest-mass density in order to consistently recover the Newtonian limit), respectively, the system of GRMHD equations can be written explicitly in conservative form. Together with the equation for the evolution of the magnetic field as measured by the Eulerian observer, equation (20), the fundamental GRMHD system of equations can be written in the following general form:

$$\frac{1}{\sqrt{-g}}\left(\frac{\partial\sqrt{\gamma}\boldsymbol{F}^0}{\partial x^0} + \frac{\partial\sqrt{-g}\boldsymbol{F}^i}{\partial x^i}\right) = \boldsymbol{S}, \tag{40}$$

where the quantities $\boldsymbol{F}^\mu$ ($\boldsymbol{F}^0$ being the state vector and $\boldsymbol{F}^i$ being the fluxes) are

$$\boldsymbol{F}^0 = \begin{bmatrix} D \\ S_j \\ \tau \\ B^k \end{bmatrix}, \tag{41}$$

$$\boldsymbol{F}^i = \begin{bmatrix} D\tilde{v}^i \\ S_j\tilde{v}^i + p^*\delta^i_j - b_j B^i/W \\ \tau\tilde{v}^i + p^* v^i - \alpha b^0 B^i/W \\ \tilde{v}^i B^k - \tilde{v}^k B^i \end{bmatrix}, \tag{42}$$

with $\tilde{v}^i = v^i - \beta^i/\alpha$. The corresponding sources $\boldsymbol{S}$ are given by

$$\boldsymbol{S} = \begin{bmatrix} 0 \\ T^{\mu\nu}\left(\dfrac{\partial g_{\nu j}}{\partial x^\mu} - \Gamma^\delta_{\nu\mu} g_{\delta j}\right) \\ \alpha\left(T^{\mu 0}\dfrac{\partial \ln\alpha}{\partial x^\mu} - T^{\mu\nu}\Gamma^0_{\nu\mu}\right) \\ 0^k \end{bmatrix}, \tag{43}$$

where $0^k \equiv (0,\ 0,\ 0)^T$. Note that the following fundamental relations hold between the four components of the magnetic field in the comoving frame, b^μ, and the three vector components B^i measured by the Eulerian observer:

$$b^0 = \frac{W B^i v_i}{\alpha}, \tag{44}$$

$$b^i = \frac{B^i + \alpha b^0 u^i}{W}. \tag{45}$$

Finally, the modulus of the magnetic field can be written as

$$b^2 = \frac{B^2 + \alpha^2 (b^0)^2}{W^2}, \tag{46}$$

where $B^2 = B^i B_i$.

3. HYPERBOLIC STRUCTURE

In § 2.3 we have written the GRMHD equations in conservative form anticipating the use of numerical methods specifically designed to solve conservation equations, as is explained in the next section. These methods strongly rely on the hyperbolic character of the equations and on the associated wave structure. Following Anile (1989), in order to analyze the hyperbolicity of the equations, it is convenient to write them in a more suitable form. If we take the set of variables $\boldsymbol{V} = (u^\mu,\ b^\mu,\ p,\ s)$, where s

is the specific entropy, the system of equations can be written as a quasi-linear system of the form

$$\mathcal{A}_B^{\mu A}\nabla_\mu V^B = 0, \tag{47}$$

where A and B run from 0 to 9, as the number of variables, and the 10×10 matrices $\mathcal{A}^\mu$ are given by

$$\mathcal{A}^\mu = \begin{pmatrix} \mathcal{C}u^\mu\delta^\alpha_\beta & -b^\mu\delta^\alpha_\beta + P^{\alpha\mu}b_\beta & l^{\alpha\mu} & 0^{\alpha\mu} \\ b^\mu\delta^\alpha_\beta & -u^\mu\delta^\alpha_\beta & f^{\mu\alpha} & 0^{\alpha\mu} \\ \rho h\delta^\mu_\beta & 0^\mu_\beta & u^\mu/c_s^2 & 0^\mu \\ 0^\mu_\beta & 0^\mu_\beta & 0^\mu & u^\mu \end{pmatrix}, \tag{48}$$

where c_s stands for the speed of sound

$$c_s^2 = \left(\frac{\partial p}{\partial e}\right)_s, \tag{49}$$

e being the mass-energy density of the fluid $e=\rho(1+\varepsilon)$. In equation (48) the following definitions are introduced:

$$\mathcal{C} = \rho h + b^2, \tag{50}$$

$$P^{\alpha\mu} = g^{\alpha\mu} + 2u^\alpha u^\mu, \tag{51}$$

$$l^{\mu\alpha} = \frac{\rho h g^{\mu\alpha} + \left(\rho h - b^2/c_s^2\right)u^\mu u^\alpha}{\rho h}, \tag{52}$$

$$f^{\mu\alpha} = \frac{u^\alpha b^\mu/c_s^2 - u^\mu b^\alpha}{\rho h}, \tag{53}$$

as well as the notation

$$0^\mu \equiv 0, \quad 0^{\alpha\mu} \equiv (0,\ 0,\ 0,\ 0)^T, \quad 0^\mu_\beta \equiv (0,\ 0,\ 0,\ 0). \tag{54}$$

If $\phi(x^\mu)=0$ defines a characteristic hypersurface of the above system (eq. [47]), the characteristic matrix, given by $\mathcal{A}^\epsilon\phi_\epsilon$, can be written as

$$\mathcal{A}^\epsilon\phi_\epsilon = \begin{pmatrix} \mathcal{C}a\delta^\mu_\nu & m^\mu_\nu & l^\mu & 0^\mu \\ \mathcal{B}\delta^\mu_\nu & -a\delta^\mu_\nu & f^\mu & 0^\mu \\ \rho h\phi_\nu & 0_\nu & a/c_s^2 & 0 \\ 0_\nu & 0_\nu & 0 & a \end{pmatrix}, \tag{55}$$

where $\phi_\mu = \nabla_\mu\phi$, $a = u^\mu\phi_\mu$, $\mathcal{B} = b^\mu\phi_\mu$, $l^\mu = l^{\mu\nu}\phi_\nu = \phi^\mu + (\rho h - b^2/c_s^2)au^\mu/\rho h + \mathcal{B}b^\mu/\rho h$, $f^\mu = f^{\mu\nu}\phi_\nu = (ab^\mu/c_s^2 - \mathcal{B}u^\mu)/\rho h$, and $m^\mu_\nu = (\phi^\mu + 2au^\mu)b_\nu - \mathcal{B}\delta^\mu_\nu$. The determinant of the matrix given by equation (55) must vanish, i.e.,

$$\det\left(\mathcal{A}^\mu\phi_\mu\right) = \mathcal{C}a^2\mathcal{A}^2\mathcal{N}_4 = 0, \tag{56}$$

where

$$\mathcal{A} = \mathcal{C}a^2 - \mathcal{B}^2, \tag{57}$$

$$\mathcal{N}_4 = \rho h\left(\frac{1}{c_s^2} - 1\right)a^4 - \left(\rho h + \frac{b^2}{c_s^2}\right)a^2G + \mathcal{B}^2G, \tag{58}$$

and $G = \phi^\mu\phi_\mu$. If we now consider a wave propagating in an arbitrary direction x with a speed λ, the normal to the characteristic hypersurface is given by the four-vector

$$\phi_\mu = (-\lambda,\ 1,\ 0,\ 0), \tag{59}$$

and by substituting equation (59) in equation (56), we obtain the so-called characteristic polynomial, whose zeros give the characteristic speed of the waves propagating in the x-direction. Three different kinds of waves can be obtained according to which factor in equation (56) becomes zero. For entropic waves $a=0$, for Alfvén waves $\mathcal{A}=0$, and for magnetosonic waves $\mathcal{N}_4=0$.

Let us next analyze in more detail the characteristic equation (56). First of all, since the four-vector ϕ_μ must be spacelike (this is a property of the RMHD system of equations; Anile 1989), it follows that $\phi^\mu\phi_\mu > 0$. In terms of the wave speed λ we obtain

$$-\alpha\sqrt{\gamma^{xx}} - \beta^x < \lambda < \alpha\sqrt{\gamma^{xx}} - \beta^x. \tag{60}$$

The characteristic speed λ of the entropic waves propagating in the x-direction, given by the solution of the equation $a=0$, is

$$\lambda = \alpha v^x - \beta^x. \tag{61}$$

For Alfvén waves, given by $\mathcal{A}=0$, there are two solutions corresponding, in general, to different speeds of the waves,

$$\lambda = \frac{b^x \pm \sqrt{\mathcal{C}}u^x}{b^0 \pm \sqrt{\mathcal{C}}u^t}. \tag{62}$$

In the case of magnetosonic waves it is, however, not possible, in general, to obtain explicit expressions for their speeds since they are given by the solutions of the quartic equation $\mathcal{N}_4=0$ with a, $\mathcal{B}$, and G explicitly written in terms of λ as

$$a = \frac{W}{\alpha}(-\lambda + \alpha v^x - \beta^x), \tag{63}$$

$$\mathcal{B} = b^x - b^0\lambda, \tag{64}$$

$$G = \frac{1}{\alpha^2}\left[-(\lambda+\beta^x)^2 + \alpha^2\gamma^{xx}\right]. \tag{65}$$

Let us note that in the previous discussion about the roots of the characteristic polynomial we have omitted the fact that the entropy waves and the Alfvén waves appear as double roots. These superfluous eigenvalues appear associated with unphysical waves and are the result of working with the unconstrained, 10×10 system of equations. We note that van Putten (1991) derived a different augmented system of RMHD equations in constrained-free form with different nonphysical waves. Any attempt to develop a numerical procedure based on the wave structure of the RMHD equations must remove these nonphysical waves (and the corresponding eigenvectors) from the wave decomposition. In the case of SRMHD Komissarov (1999) and Koldoba et al. (2002) eliminate the nonphysical eigenvectors by demanding the waves to preserve the values of the invariants $u^\mu u_\mu = -1$ and $u^\mu b_\mu = 0$ as suggested by Anile (1989). Correspondingly, Balsara (2001) selects the physical eigenvectors by comparing with the equivalent expressions in the nonrelativistic limit.

It is worth noticing that just as in the classical case, the relativistic MHD equations have degenerate states in which two or more wave speeds coincide, which breaks the strict hyperbolicity of the system. Komissarov (1999) has reviewed the properties of these degeneracies. In the fluid rest frame, the degeneracies in both classical and relativistic MHD are the same: either the slow and Alfvén waves have the same speed as the entropy wave when propagating perpendicularly to the magnetic field (degeneracy I), or the slow wave, the fast wave, or both have the same speed as the

Alfvén wave when propagating in a direction aligned with the magnetic field (degeneracy II). L. Antón et al. (2006, in preparation) have characterized these degeneracies in terms of the components of the magnetic field four-vector normal and tangential to the Alfvén wave front, $\boldsymbol{b}_n$, $\boldsymbol{b}_t$. When $\boldsymbol{b}_n = 0$, the system falls within degeneracy I, while degeneracy II is reached when $\boldsymbol{b}_t = 0$. Let us note that the previous characterization is covariant (i.e., defined in terms of four-vectors) and hence can be checked in any reference frame. In addition, Antón et al. have also worked out a single set of right and left eigenvectors that are regular and span a complete basis in any physical state, including degenerate states. The *renormalization* procedure can be understood as a relativistic generalization of the work performed by Brio & Wu (1988) in classical MHD. This procedure avoids the ambiguity inherent to a change of basis when approaching a degeneracy, as done, e.g., by Komissarov (1999). The renormalized eigenvectors have been used in all the tests reported in the present paper using the *full-wave decomposition* Riemann solver.

4. NUMERICAL APPROACH

Writing the GRMHD equations as a first-order, flux-conservative, hyperbolic system allows us to use numerical methods specifically designed to solve such kinds of equations. Among these methods, HRSC schemes are recognized as the most efficient schemes to evolve complex flows accurately, capturing the discontinuities that appear when dealing with nonlinear hyperbolic equations.

4.1. *Integral Form of the GRMHD Equations*

To apply HRSC techniques to the present GRMHD system, we use equation (40) in integral form. Let Ω be a simply connected region of the four-dimensional manifold bounded by a closed three-dimensional surface $\partial\Omega$. We take $\partial\Omega$ as the standard-oriented hyperparallelepiped made up of the two spacelike surfaces Σ_t, $\Sigma_{t+\Delta t}$ plus timelike surfaces Σ_{x^i}, $\Sigma_{x^i+\Delta x^i}$, which connect the two temporal slices. Then, the integral form of equation (40) is

$$\int_\Omega \frac{1}{\sqrt{-g}}\frac{\partial\sqrt{\gamma}\boldsymbol{F}^0}{\partial x^0}\,d\Omega + \int_\Omega \frac{1}{\sqrt{-g}}\frac{\partial\sqrt{-g}\boldsymbol{F}^i}{\partial x^i}\,d\Omega = \int_\Omega \boldsymbol{S}\,d\Omega, \tag{66}$$

which can be written, for numerical purposes, as

$$\begin{aligned}
&\left(\bar{\boldsymbol{F}}^0\right)_{t+\Delta t} - \left(\bar{\boldsymbol{F}}^0\right)_t = \\
&-\left(\int_{\Sigma_{x^1+\Delta x^1}} \sqrt{-g}\hat{\boldsymbol{F}}^1\,dx^0\,dx^2\,dx^3 - \int_{\Sigma_{x^1}} \sqrt{-g}\,\hat{\boldsymbol{F}}^1\,dx^0\,dx^2\,dx^3\right) \\
&-\left(\int_{\Sigma_{x^2+\Delta x^2}} \sqrt{-g}\,\hat{\boldsymbol{F}}^2\,dx^0\,dx^1\,dx^3 - \int_{\Sigma_{x^2}} \sqrt{-g}\,\hat{\boldsymbol{F}}^2\,dx^0\,dx^1\,dx^3\right) \\
&-\left(\int_{\Sigma_{x^3+\Delta x^3}} \sqrt{-g}\,\hat{\boldsymbol{F}}^3\,dx^0\,dx^1\,dx^2 - \int_{\Sigma_{x^3}} \sqrt{-g}\,\hat{\boldsymbol{F}}^3\,dx^0\,dx^1\,dx^2\right) \\
&+\int_\Omega \boldsymbol{S}\,d\Omega,
\end{aligned} \tag{67}$$

$$\bar{\boldsymbol{F}}^0 = \frac{1}{\Delta V}\int_{x^1}^{x^1+\Delta x^1}\int_{x^2}^{x^2+\Delta x^2}\int_{x^3}^{x^3+\Delta x^3} \sqrt{\gamma}\boldsymbol{F}^0\,dx^1\,dx^2\,dx^3, \tag{68}$$

and

$$\Delta V = \int_{x^1}^{x^1+\Delta x^1}\int_{x^2}^{x^2+\Delta x^2}\int_{x^3}^{x^3+\Delta x^3} \sqrt{\gamma}\,dx^1\,dx^2\,dx^3. \tag{69}$$

The carets appearing on the fluxes denote that these fluxes, which are calculated at cell interfaces where the flow conditions can be discontinuous, are obtained by solving Riemann problems between the corresponding numerical cells. These numerical fluxes are further discussed in § 4.3.

We note that in order to increase the spatial accuracy of the numerical solution, the primitive variables (see § 4.5) are reconstructed at the cell interfaces before the actual computation of the numerical fluxes. We use a standard second-order minmod reconstruction procedure to compute the values of p, ρ, v_i, and B^i ($i = 1, 2, 3$) at both sides of each numerical interface. However, when computing the numerical fluxes along a certain direction, we do not allow for discontinuities in the magnetic field component along that direction. Furthermore, the equations in integral form are advanced in time using the method of lines in conjunction with a second-order, conservative Runge-Kutta method (Shu & Osher 1988).

4.2. *Induction Equation*

The main advantage of the above numerical procedure, equation (67), to advance in time the system of equations is that those variables that obey a conservation law are, by construction, conserved during the evolution as long as the balance between the fluxes at the boundaries of the computational domain and the source terms is zero. This is an important property that a hydrodynamics code should fulfill.

However, as far as the magnetic field components are concerned, the system of equations given by equation (40) only includes the induction equation, equation (22), expressed by equation (40) in conservation form, while the divergence-free condition, equation (19), remains as an additional constraint to be imposed. Therefore, the numerical advantage of using equation (67) for the conserved variables does not apply straightforwardly for the magnetic field components. Indeed, there is no guarantee that the divergence is conserved numerically when updating the magnetic field if we were to use the same numerical procedure we employ for the rest of the components of the state vector.

Among the methods designed to preserve the divergence of the magnetic field, we use the constrained transport method designed by Evans & Hawley (1988) and first extended to HRSC methods by Ryu et al. (1998; for a recent discussion see also Londrillo & del Zanna 2004). This scheme is based on the use of the Stokes theorem after the integration of the induction equation on surfaces of constant t and x^i, Σ_{t,x^i}. Let us write equation (22) as

$$\frac{1}{\sqrt{\gamma}}\frac{\partial\vec{\mathcal{B}}}{\partial t} = \vec{\nabla}\times\vec{\Omega}, \tag{70}$$

where we have defined the density vector $\vec{\mathcal{B}} = \sqrt{\gamma}\vec{B}$ and $\vec{\Omega} = (\alpha\vec{v} - \vec{\beta})\times\vec{B}$.

To obtain a discretized version of equation (70), we proceed as follows. At a given time, each numerical cell is bounded by six two-surfaces. Consider, for concreteness, the two-surface Σ_{t,x^3}, defined by $t = \text{const}$ and $x^3 = \text{const}$, and the remaining two coordinates spanning the intervals from x^1 to $x^1 + \Delta x^1$ and from

x^2 to $x^2 + \Delta x^2$. The magnetic flux through this two-surface is given by

$$\Phi_{\Sigma_{t,x^3}} = \int_{\Sigma_{t,x^3}} \vec{B} \cdot d\vec{\Sigma}. \tag{71}$$

Furthermore, the electromotive force $\mathcal{E}$ around the contour $\partial(\Sigma_{t,x^3})$ is defined as

$$\mathcal{E}(t) = -\int_{\partial(\Sigma_{t,x^3})} \Omega_i \, dx^i. \tag{72}$$

Integrating equation (70) on the two-surface Σ_{t,x^3} and applying the Stokes theorem to the right-hand side, we obtain the equation

$$\frac{d\Phi_{\Sigma_{t,x^3}}}{dt} = -\mathcal{E} = \int_{\partial(\Sigma_{t,x^3})} \Omega_i \, dx^i, \tag{73}$$

which can be integrated to give

$$\Phi^{t+\Delta t}_{\Sigma_{t,x^3}} - \Phi^{t}_{\Sigma_{t,x^3}} = \int_t^{t+\Delta t} \int_{\partial(\Sigma_{t,x^3})} \hat{\Omega}_i \, dx^i \, dt, \tag{74}$$

where the caret denotes again that quantities $\hat{\Omega}_i$ are calculated at the edges of the numerical cells, where they can be discontinuous. At each edge, as we describe below, these quantities are calculated using the solution of four Riemann problems between the corresponding faces whose intersection defines the edge. However, irrespective of the expression we use for calculating $\hat{\Omega}_i$, the method to advance the magnetic fluxes at the faces of the numerical cells satisfies, by construction, the divergence constraint. To see this, we can integrate over a computational cell the divergence of the magnetic field at a given time. After applying the Gauss theorem, we obtain

$$\int_{\Delta V} \nabla \cdot \vec{B} \, dV = \int_{\Sigma} \vec{B} \cdot d\vec{\Sigma} = \sum_{\text{faces},\, i=1}^{6} \Phi_i. \tag{75}$$

In the previous expression, ΔV stands for the volume of a computational cell, whereas Σ denotes the closed surface bounding that cell. The summation is extended to the six faces (coordinate surfaces) shaping Σ. Now, taking the time derivative of equation (75) yields

$$\begin{aligned} \frac{d}{dt} \int_{\Delta V} \nabla \cdot \vec{B} \, dV &= -\sum_{\text{faces},\, i=1}^{6} \frac{d}{dt} \Phi_i \\ &= \sum_{\text{faces},\, i=1}^{6} \sum_{\text{edges},\, j=1}^{4} \mathcal{E}_{ij}, \end{aligned} \tag{76}$$

where $\mathcal{E}_{ij}$ is the contribution from edge j to the total electromotive force around the contour defined by the boundary of face i. It turns out that the above summation cancels exactly since the value of $\mathcal{E}$ for the common edge of two adjacent faces has a different sign for each face. Therefore, if the initial fluxes through each face of a numerical cell verify $\Sigma^6_{\text{faces},i=1} \Phi_i = 0$, this condition will be fulfilled during the evolution.

4.3. *Numerical Fluxes and Divergence-free Condition*

The numerical integration of the GRMHD equations, equation (40) or equation (67), is done using an HRSC scheme. Such schemes are specifically designed to solve nonlinear hyperbolic systems of conservation laws (LeVeque 1998; Toro 1997). They are written in conservation form and use approximate or exact Riemann solvers to compute the numerical fluxes between neighboring grid zones. This fact guarantees the proper capturing of all discontinuities that may arise naturally in the solution space of a nonlinear hyperbolic system. Applications of HRSC schemes in relativistic hydrodynamics can be found in Martí & Müller (2003) and Font (2003). Incidentally, we note that a detailed description of linearized Riemann solvers based on the spectral decomposition can be found in Font et al. (1994) for special relativistic hydrodynamics and in Banyuls et al. (1997) (diagonal metrics), Font et al. (2000), and Ibáñez et al. (2001) (general metrics) for general relativistic hydrodynamics. For HRSC methods in classical MHD, on the other hand, we refer to Ryu et al. (1995, 1998).

As discussed in § 3, the existence of degeneracies in the eigenvectors of the RMHD system of equations makes it hazardous to implement linearized Riemann solvers based on the full spectral decomposition of the flux vector Jacobians. Nevertheless, we have succeeded in developing and implementing in the code a full-wave decomposition (Roe type) Riemann solver based on a single, renormalized set of right and left eigenvectors, as discussed in detail in L. Antón et al. (2006, in preparation), which is regular for any physical state, including degeneracies. This Riemann solver is invoked in the code after a (local) linear coordinate transformation based on the procedure developed by Pons et al. (1998) that allows one to use special relativistic Riemann solvers in general relativity and has been properly extended to include magnetic fields (see § 4.4).

In addition to the Roe-type Riemann solver, we also use two simpler alternative approaches to compute the numerical fluxes, namely, the HLL single-state Riemann solver of Harten et al. (1983) and the second-order central (symmetric) scheme of Kurganov & Tadmor (2000; hereafter KT scheme). The KT scheme has proved recently to yield results with an accuracy comparable to those provided by full-wave decomposition Riemann solvers in simulations involving purely hydrodynamical special relativistic flows (Lucas-Serrano et al. 2004) and general relativistic flows in dynamical neutron star spacetimes (Shibata & Font 2005). The interested reader is referred to Kurganov & Tadmor (2000) and Lucas-Serrano et al. (2004) for specific details on the KT central scheme.

Correspondingly, the HLL Riemann solver is based on the calculation of the maximum and the minimum left- and right-propagating wave speeds emanating at the interface between the two initial states, and the resulting flux is given by

$$\hat{\boldsymbol{F}}(\boldsymbol{U}_L, \boldsymbol{U}_R) = \frac{\tilde{\lambda}_+ \boldsymbol{F}(\boldsymbol{U}_L) - \tilde{\lambda}_- \boldsymbol{F}(\boldsymbol{U}_R) + \tilde{\lambda}_+ \tilde{\lambda}_- (\boldsymbol{U}_R - \boldsymbol{U}_L)}{\tilde{\lambda}_+ - \tilde{\lambda}_-}, \tag{77}$$

where $\tilde{\lambda}_\pm = \lambda_\pm / \alpha$. Quantities $\hat{\boldsymbol{F}}$ stand for the numerical fluxes along each of the three spatial coordinate directions, namely, $\hat{\boldsymbol{F}}^i$ ($i = 1, 2, 3$) in equation (40), whereas $\boldsymbol{U} \equiv \boldsymbol{F}^0$ denotes the state vector. Subindices L and R stand for the left and right states defining the Riemann problems at each numerical interface. Moreover, λ_- and λ_+ are upper bounds of the speeds of the left- and right-propagating waves emanating from the cell interface,

$$\lambda_+ = \max\left(0,\ \lambda^+_{\text{fms},L},\ \lambda^+_{\text{fms},R}\right), \tag{78}$$

$$\lambda_- = \min\left(0,\ \lambda^-_{\text{fms},L},\ \lambda^-_{\text{fms},R}\right), \tag{79}$$

where $\lambda^s_{\mathrm{fms},I}$ stands for the wave speed of the fast magnetosonic wave propagating to the left ($s = -$) or to the right ($s = +$) computed at state I (=L, R). These speeds are obtained by looking for the smallest and largest solution of the quartic equation $\mathcal{N}_4 = 0$ and can be effectively computed with a Newton-Raphson iteration scheme starting from $\lambda = \pm\alpha(\gamma^{ii})^{1/2} - \beta^i$ ($i = 1, 2, 3$).

Any of the flux formulae we have discussed can be used to advance the hydrodynamic variables according to equation (67) and also to calculate the quantities $\hat{\Omega}_i$ needed to advance in time the magnetic fluxes following equation (74). At each edge of the numerical cell, $\hat{\Omega}_i$ is written as an average of the numerical fluxes calculated at the interfaces between the faces whose intersection defines the edge. Let us consider, for illustrative purposes, $\hat{\Omega}_x$. If the indices (j, k, l) denote the center of a numerical cell, an x-edge is defined by the indices $(j,\ k+\frac{1}{2},\ l+\frac{1}{2})$. By definition, $\Omega_x = \alpha(\tilde{v}^y B^z - \tilde{v}^z B^y)$. Since

$$F^y(B^z) = \tilde{v}^y B^z - \tilde{v}^z B^y \tag{80}$$

and

$$F^z(B^y) = \tilde{v}^z B^y - \tilde{v}^y B^z, \tag{81}$$

we can express $\hat{\Omega}_x$ in terms of the fluxes as follows:

$$\hat{\Omega}_{xj,k+1/2,l+1/2} = \tfrac{1}{4}\left(\hat{F}^y_{j,k+1/2,l} + \hat{F}^y_{j,k+1/2,l+1} - \hat{F}^z_{j,k,l+1/2} - \hat{F}^z_{j,k+1,l+1/2}\right), \tag{82}$$

where $\hat{F}^y$ ($\hat{F}^z$) refers to the numerical flux in the y (z) direction corresponding to the equation for B^z (B^y) and multiplied by α to account for the correct definition of Ω. Also note that in the numerical implementation of the constraint transport method, a slightly different procedure can be followed (Ryu et al. 1998). According to this procedure, in the computation of the numerical fluxes given by equations (80) and (81), only the terms advecting the magnetic field are considered (i.e., the first term on the right-hand side of eqs. [80] and [81]), while the average in equation (82) is obtained dividing by a factor of 2 instead of 4. Both of these procedures, the one described through equations (80)–(82) and its modification provided by Ryu et al. (1998), allow us to advance the magnetic flux at the faces of the numerical cells in the correct way. Let us point out that, unlike Ryu et al. (1998), our implementation provides only one-half of the dissipation of the one-dimensional scheme when applied to plane-parallel, grid-aligned flows. Nevertheless, and despite the doubts raised by Gardiner & Stone (2005) concerning the stability of this approach, we have found that, at least for the two-dimensional tests shown here, our implementation is generally more robust. We refer the interested reader to Tóth (2000) for additional properties of the Ryu et al. (1998) scheme.

However, we need also to know the value of the magnetic field at the center of the cells in order to obtain the primitive variables after each time step (see § 4.5) and to compute again the numerical fluxes of the other conserved variables for the next time step. If $\hat{B}^x_{j\pm1/2,k,l}$ is the x-component of the magnetic field at the interface $(j \pm \frac{1}{2},\ k,\ l)$, then the x-component of the magnetic field at the center of the (j, k, l) cell, $B^x_{j,k,l}$, is obtained by taking the arithmetic average of the corresponding fluxes, i.e.,

$$B^x_{j,k,l} = \frac{1}{2}\frac{\hat{B}^x_{j-1/2,k,l}\Delta S^x_{j-1/2,k,l} + \hat{B}^x_{j+1/2,k,l}\Delta S^x_{j+1/2,k,l}}{\Delta S^x_{j,k,l}}, \tag{83}$$

where $\Delta S^x_{j\pm1/2,k,l}$ is the area of the interface surface between two adjacent cells, located at $x_{j\pm1/2}$ and bounded between $[y_{k-1/2},\ y_{k+1/2}]$ and $[z_{l-1/2},\ z_{l+1/2}]$. Analogous expressions for $\hat{\Omega}_{yj+1/2,k,l+1/2}$ and $\hat{\Omega}_{zj+1/2,k+1/2,l}$ and for $B^y_{j,k,l}$ and $B^z_{j,k,l}$ can be easily derived.

4.4. *Special Relativistic Riemann Solvers in GRMHD*

In Pons et al. (1998) we presented a general procedure to use any Riemann solver designed for the special relativistic hydrodynamics equations in a general relativistic framework. In this section we describe a generalization of this approach to account for the magnetic field. It will be used to compute the numerical fluxes from the special relativistic full-wave decomposition Riemann solver discussed above. The procedure is based on performing linear transformations to locally flat (or geodesic) systems of coordinates at each numerical cell interface, from which the metric becomes locally Minkowskian (plus second-order terms). Notice that this approach is equivalent to the usual approach in classical fluid dynamics where one uses the solution of Riemann problems in slab symmetry for problems in cylindrical or spherical coordinates.

In order to generalize this procedure to the GRMHD case, one must start remembering that in the pure hydrodynamical case, the components of the shift vector transversal to the cell interface play the role of a *grid* velocity, i.e., as if we have a moving interface. As discussed in detail in Pons et al. (1998), this can be easily understood by noticing that the fluxes through the moving interface for the local observer can be written as $\bar{F}^i - (\beta^i/\alpha)F^0$, where $\bar{F}^i$ are the fluxes when $\beta^i = 0$ and F^0 is the corresponding state vector. In terms of D, S_j, τ, and p^*, the structure of the first five flux components given by equation (42) in the magnetic case follows the previous discussion with the conserved quantities advected with $\tilde{v}^i$ (which includes the correction term for the moving grid) and extra terms in the fluxes of momentum and energy (which do not depend explicitly on the shift vector). This allows one to proceed along the same steps as in Pons et al. (1998): (1) introduce the locally Minkowskian coordinate system at each interface, (2) solve the Riemann problem to obtain the numerical fluxes through the moving grid as seen by the locally Minkowskian observer, and (3) invert the transformation to obtain the numerical fluxes in the original coordinates.

Let us now concentrate on the last three components of the fluxes given by equation (42), namely, $\tilde{v}^i B^k - \tilde{v}^k B^i$, corresponding to the evolution of the magnetic field. The terms $\tilde{v}^i B^k - v^k B^i$ also follow the discussion for the nonmagnetic case and the same numerical procedure can then be applied. However, the term $\beta^k B^i/\alpha$ couples the components of the shift vector parallel to the cell interface to the perpendicular magnetic field. This term has to be interpreted as a correction to the total electromotive force caused by the movement of the surface with respect to the Eulerian observer and has to be added to the final expression for the flux.

In § 5 the validity of this approach with a full-wave decomposition Roe-type Riemann solver is assessed in a series of tests including discontinuous initial value problems, steady flows, and dynamical accretion disks. As a result of this assessment, we conclude that the generalized procedure to use SR Riemann solvers in multidimensional GRMHD is an efficient and robust alternative to develop specific solvers that need the knowledge of the whole spectral decomposition (eigenvalues and eigenvectors) in general relativity. Since each local change of coordinates is linear and it only involves a few arithmetical operations, the additional computational cost of the approach is negligible.

4.5. *Primitive Variable Recovering*

The numerical procedure used to solve the GRMHD equations allows us to obtain the values of the conserved variables $\boldsymbol{F}^0$ at time $t + \Delta t$ from their values at time t. However, the values of the physical variables (i.e., ρ, ϵ, etc.) are also needed at each time step in order to compute the fluxes. It is therefore necessary to solve the algebraic equations relating the conserved and the physical variables. For the classical MHD equations and an ideal gas equation of state the physical variables can be expressed as explicit functions of the conserved ones. Unfortunately, this cannot be done in GRMHD, a feature shared by the special and general relativistic versions of the purely hydrodynamics equations within the 3+1 approach (for an alternative formulation without this shortcoming see Papadopoulos & Font 2000). Therefore, the resulting nonlinear algebraic system of equations has to be solved numerically. The procedure we describe below is an extension to full general relativity of that developed by Komissarov (1999) in the special relativistic case.

The basic idea of this procedure relies on the fact that it is not necessary to solve the system of equations (37)–(39) for the three components of the momentum, but instead for its modulus $S^2 = S^i S_i$. The next step is to eliminate the components of b^α through equations (44) and (45). After some algebra it is possible to write S^2 as

$$S^2 = \left(Z + B^2\right)^2 \frac{W^2 - 1}{W^2} - \left(2Z + B^2\right) \frac{\left(B^i S_i\right)^2}{Z^2}, \quad (84)$$

where $Z = \rho h W^2$.

The equation for the total energy can be worked out in a similar way:

$$\tau = Z + B^2 - p - \frac{B^2}{2W^2} - \frac{\left(B^i S_i\right)^2}{2Z^2} - D. \quad (85)$$

Equations (37), (84), and (85), together with the definition of Z, form a system for the unknowns ρ, p, and W, assuming that the function $h = h(\rho,\ p)$ is provided. In our calculations we restrict ourselves to both an ideal gas equation of state (EOS), $p = \rho\epsilon(\gamma - 1)$, for which $h = 1 + \gamma p/\rho(\gamma - 1)$, where γ is the adiabatic index, and a polytropic EOS (valid to describe isoentropic flows), $p = K\rho^\gamma$, where K is the polytropic constant. In this last case the integration of the total energy equation can be avoided and the equation for the specific enthalpy is given by

$$h = 1 + \frac{\gamma K}{\gamma - 1} \rho^{\gamma - 1}. \quad (86)$$

Then equations (37) and (84) are solved to obtain ρ and W.

5. RESULTS

We now assess the formulation of the GRMHD equations we have presented, as well as the numerical techniques we employ to solve them. The simulations reported in this section are introduced in a way that gradually increases the level of complexity of the flow to solve, starting first with shock tube tests in purely Minkowski spacetimes with or without constant gauge terms. Next we turn to one-dimensional tests of accreting magnetized flows onto Schwarzschild and Kerr black holes, to finally discuss two-dimensional simulations of thick accretion disks orbiting around black holes. This collection of tests allows us to validate our approach by comparing the numerical simulations with analytic solutions (in the cases where such a comparison is possible), investigating the ability of the code to preserve stationary solutions in the strong gravitational field regime, and comparing with available numerical results reported in the literature.

For those tests that involve (background) black hole spacetimes we adopt Boyer-Lindquist coordinates and fix the unit of length to $r_g \equiv M$, M being the mass of the black hole.

5.1. *Relativistic Brio-Wu Shock Tube Test*

The first test is the relativistic analog of the classical Brio-Wu shock tube problem (Brio & Wu 1988; Balsara 2001), as adapted to the relativistic MHD case by van Putten (1993). The computational setup consists of two constant states that are initially at rest and separated through a discontinuity placed at the middle point of a unit length domain. The two states are characterized by the following initial conditions: (1) $\rho = 1.0$, $v^x = 0.0$, $v^y = 0.0$, $p = 1.0$, and $B^y = 1.0$ (left state); and (2) $\rho = 0.125$, $v^x = 0.0$, $v^y = 0.0$, $p = 0.10$, and $B^y = -1.0$ (right state). The adiabatic index of the ideal gas EOS is $\gamma = 2$, and the x component of the magnetic field is equal for both left and right states, $B^x = 0.5$. The test is performed using a Cartesian grid with 1600 cells. Results are reported for the HLL Riemann solver (as the other two schemes yield similar results) and for a CFL parameter equal to 0.5.

The results of the simulation are shown in Figure 1, which displays the wave structure for various quantities after the removal of the membrane. This wave structure comprises a fast rarefaction wave, a slow compound wave (both moving to the left), a contact discontinuity, and, moving to the right, a slow shock wave and a fast rarefaction wave. The short-dashed line in the six panels of Figure 1 shows the wave pattern produced in the purely Minkowski spacetime at time $t = 0.4$. It is in good overall agreement with the results obtained by Balsara (2001), in particular regarding the location of the different waves, the maximum value achieved by the Lorentz factor ($W = 1.457$), and the smearing of the numerical solution. In addition to this solution, we use open circles to denote the results of this test in flat spacetime but incorporating *gauge* effects by selecting a value of the lapse function different from unity, namely, $\alpha = 2$. The solution, which is shown at $t = 0.2$, matches as expected with that represented by the short-dashed line, obtained in flat spacetime at time $t = 0.4$. Finally, the open squares refer to a third version of this test carried out in a flat spacetime with a nonvanishing shift vector, namely, $\beta^x = 0.4$. The numerical displacement that is thus produced is in perfect agreement with the expected one. This is emphasized in the figure by translating the short-dashed line into the long-dashed one by the predicted amount, $\beta^x t = 0.16$.

5.2. *Magnetized Spherical Accretion*

In the second test we check the ability of the code to numerically maintain with a time-dependent system of equations the stationarity of the spherically symmetric accretion solution of a perfect fluid onto a Schwarzschild black hole in the presence of a radial magnetic field. It is worth emphasizing that the only consistent solution for magnetized spherical accretion with a force-free magnetic field satisfying the whole set of Maxwell equations corresponds to the one with $\mathcal{J} = 0$ (see Appendix A for a proof). However, it is easy to show that any magnetic field of the type $b^\alpha = (b^t,\ b^r,\ 0,\ 0)$ does not affect the spherically symmetric hydrodynamical solution. Therefore, although the resulting configuration is nonphysical, it provides a useful numerical test and has been used in the literature for this purpose (Gammie et al. 2003; De Villiers & Hawley 2003a; Duez et al. 2005).

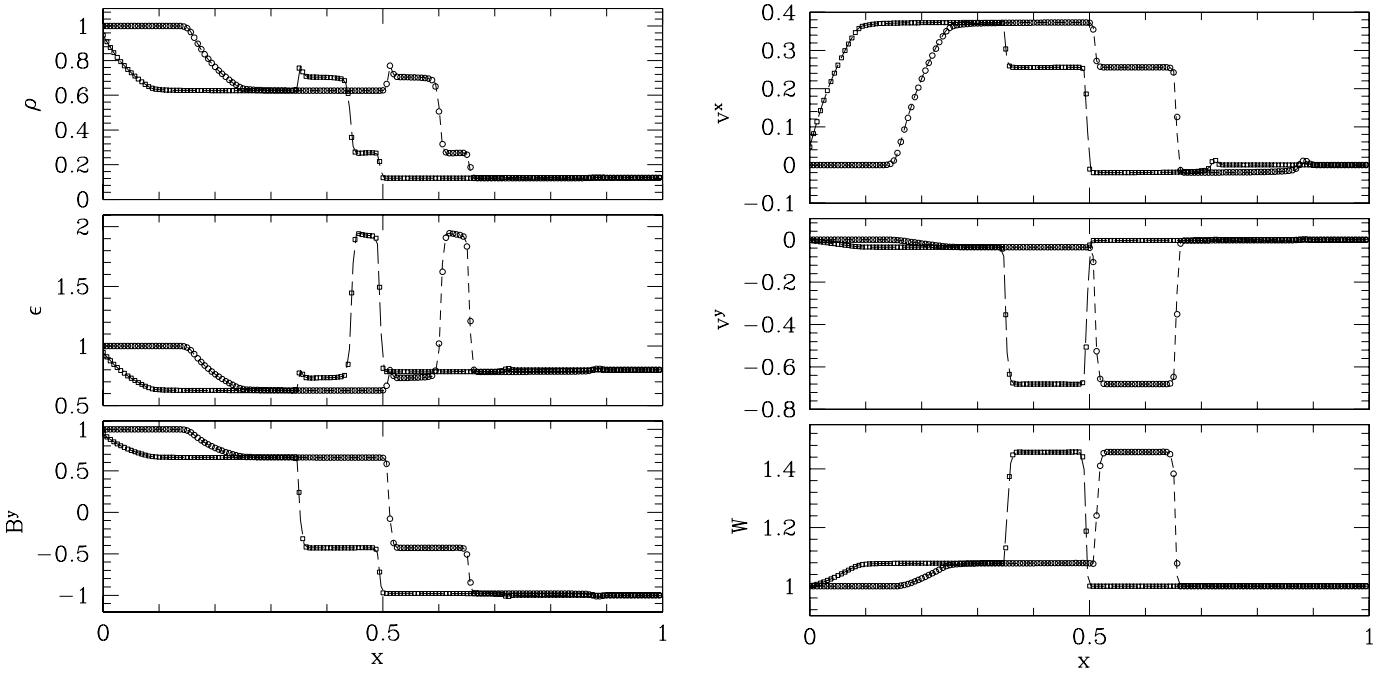

FIG. 1.—Wave pattern of the relativistic version of the Brio-Wu shock tube test. The left panels report the rest-mass density ρ, the specific internal energy ϵ, and the y component of the magnetic field B^y, while the right panels report the x and y components of the velocity v^x and v^y and the Lorentz factor W. The short-dashed line shows the solution at time $t = 0.4$ in Minkowski spacetime. The open circles represent the solution at time $t = 0.2$ in Minkowski spacetime with gauge effects mimicked by a lapse function $\alpha = 2.0$. The open squares represent the solution at time $t = 0.4$ in Minkowski spacetime with a shift vector $\beta^x = 0.4$, while the long-dashed line is the translation of the short-dashed one by the amount $\beta^x t = 0.16$. (Only 160 of the 1600 data points used in the simulation are drawn.)

The initial setup consists of a perfect isoentropic fluid obeying a polytropic EOS with $\gamma = 4/3$. The critical radius of the solution is located at $r_c = 8.0$, and the rest-mass density at the critical radius is $\rho_c = 6.25 \times 10^{-2}$. These parameters suffice to provide the full description of the spherical accretion onto a Schwarzschild black hole as described in detail by Michel (1972). The radial magnetic field component, which can in principle follow any radial dependence, is chosen to satisfy the divergence-free condition. Moreover, its strength is characterized by the ratio $\beta = b^2/2p$ between the magnetic pressure and the gas pressure, computed at the critical radius of the flow. These initial conditions are evolved in time using the Roe-type Riemann solver described in § 4.4 on a uniform radial grid covering the region between $r_{\min} = r_{\text{horizon}} + \delta$ and $r_{\max} = 10.0$, where δ varies from 0.1 to 0.3.

Figure 2 shows the comparison between the analytic solution (*solid lines*) and the numerical solution (*circles*) for one representative case with pressure ratio $\beta = 1.0$ and $\delta = 0.3$. These results are obtained with a numerical grid of $N = 100$ radial zones, for which convergence is reached at time $t = 250M$. The order of accuracy of the code is computed by monitoring the error $L \equiv \sum_{i=1}^{N} |Q_i - Q_{a,i}| / \sum_{i=1}^{N} Q_{a,i}$ for quantity $Q = \rho$ as the number of grid points N is increased, where Q_a represents the analytic solution. This procedure is repeated for different values of the ratio β, namely, for $\beta = 0$, 1, 10, 100, and 1000, and the results, which are reported in Figure 3, show that the global order of convergence of the code is 2, irrespective of the parameter β.

A comparison of the accuracy of the three methods we use to compute the numerical fluxes is reported in Table 1, for $\beta = 10.0$ and $N = 70$ radial zones. The results for the magnetized spherical accretion test appear in the upper half of the table. This table reports the global error of some representative quantities when numerical convergence is reached. For the particular test discussed in this section we find that there is not a single method providing the smallest error in all of the quantities, and the Roe-type solver, which is the most accurate in the computation of the hydrodynamic variables, is the least accurate in the computation of the magnetic field.

5.3. *Equatorial Kerr Accretion*

A further one-dimensional test of the code is provided by the stationary magnetized inflow solution in the Kerr metric derived by Takahashi et al. (1990). This solution was subsequently adapted to the case of equatorial inflow in the region between the black hole horizon and the marginally stable orbit by Gammie (1999). This test has been used by De Villiers & Hawley (2003a) and Gammie et al. (2003) in the validation of their GRMHD codes. It represents a step forward in the level of complexity of the equations to solve with respect to those used in the previous two sections, since the test involves the Kerr metric, albeit specialized to the equatorial plane. As a result, additional terms due to the increased number of nonvanishing Christoffel symbols appear in the equations.

As described by Gammie (1999) and adopting his notation, the inflow solution is determined once four conserved quantities are specified, namely, the accretion rate F_M, the angular momentum flux F_L, the energy flux F_E, and the component $F_{\theta\phi}$ of the electromagnetic tensor, which is related to the magnetic flux through the inner edge of the disk. For the sake of comparison, we consider an initial setup with the same numerical values used by Gammie et al. (2003), namely, a Kerr black hole with spin parameter $a = 0.5$, $F_M = -1.0$, $F_L = -2.815344$, $F_E = -0.908382$, and $F_{\theta\phi} = 0.5$.

The numerical grid consists of $N_r \times N_\theta$ grid points in the radial and angular directions, respectively. The radial grid covers the region between $r_{\min} = r_{\text{horizon}} + 0.2$ and $r_{\max} = 4.0$, while the angular grid consists of $N_\theta = 3$ grid points subtending a small angle of $10^{-5}\pi$ across the equatorial plane. The radial profiles of some significant variables, obtained with the Roe-type Riemann solver, are reported in Figure 4 for a radial grid of $N_r = 100$ zones. The open circles indicate the numerical results, while the underlying solid lines correspond to the analytic solution. It is found that the

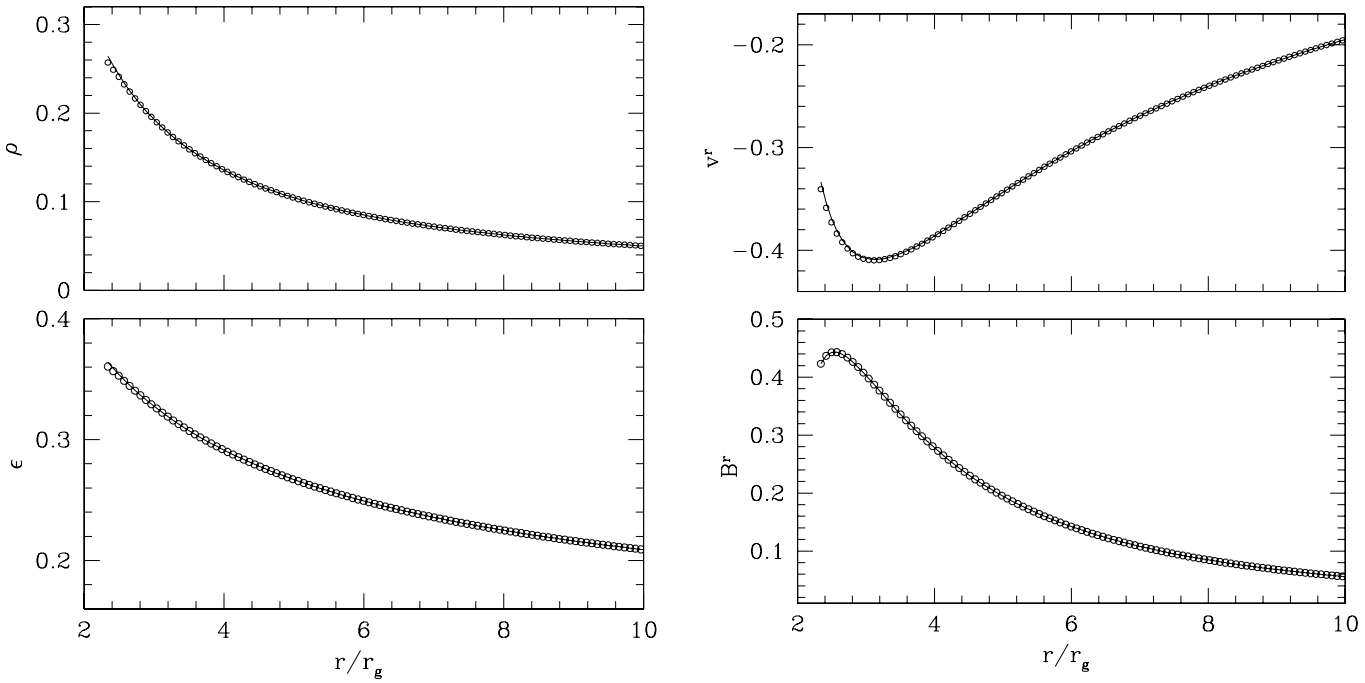

FIG. 2.—Magnetized spherical accretion. The plot shows a comparison between the analytic solution (*solid line*) and the numerical solution obtained with the Roe-type Riemann solver (*circles*) for a model with $\beta = 1.0$ and $N = 100$, once convergence is reached. The left panels display the radial profiles of the rest-mass density ρ (*top*) and the specific internal energy ϵ (*bottom*), while the right panels show the corresponding profiles for the coordinate velocity v^r (*top*) and the radial component of the magnetic field B^r (*bottom*), all of them in geometrized units.

stationarity of the solution is preserved to high accuracy by the numerical code. For the long-term evolutions considered there are no significant deviations from the analytic profiles.

As we did for the magnetized spherical accretion test, we use the current test to compute again the order of convergence of the code as the grid is refined. The global order of convergence for some representative quantities is reported in Figure 5, which shows that the code is second-order accurate. As already commented by Gammie et al. (2003), the worsening of the order of convergence for B^ϕ at high grid resolution is due to the fact that the initial condition is "semianalytic," requiring the solution of an algebraic equation. Thus, the inaccuracies produced at time $t = 0$ become more pronounced for large numbers of radial zones N_r.

The performance of the code using the HLL and KT solvers has also been checked with this test. While the order of convergence is preserved irrespective of the numerical schemes used to compute the fluxes, the actual accuracy can vary significantly. The results of this comparison for the equatorial Kerr accretion solution are summarized in the lower half of Table 1, which reports the global error of representative quantities, when convergence is reached, on a numerical grid with $N_r = 60$ radial points.

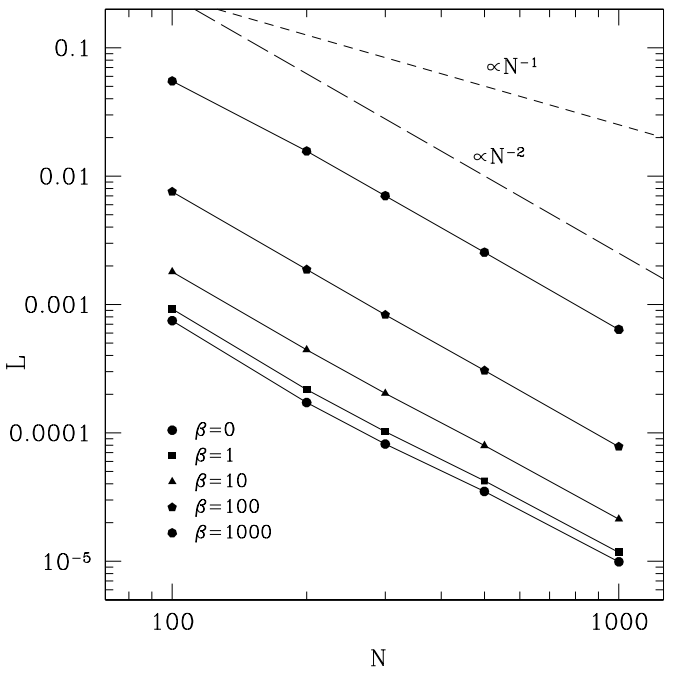

FIG. 3.—Error L of the rest-mass density (see text for definition) for the magnetized spherical accretion test when the grid resolution is increased. The short-dashed and long-dashed lines indicate first and second order of global convergence, respectively. The symbols denote different values of the magnetization parameter at the critical point.

TABLE 1
COMPARISON AMONG DIFFERENT SCHEMES

Solver	$\delta\rho$	δv^r	δB^r	δB^ϕ
Michel Test				
HLL	3.76×10^{-3}	3.92×10^{-3}	7.64×10^{-17}	...
Roe type	2.97×10^{-3}	3.45×10^{-3}	1.09×10^{-12}	...
KT	3.36×10^{-3}	3.54×10^{-3}	1.94×10^{-18}	...
Gammie Test				
HLL	1.92×10^{-2}	2.54×10^{-3}	2.28×10^{-9}	1.48×10^{-3}
Roe type	6.90×10^{-3}	3.01×10^{-3}	3.96×10^{-3}	2.14×10^{-3}
KT	1.63×10^{-2}	9.72×10^{-4}	2.30×10^{-9}	9.89×10^{-3}

NOTES.—Accretion tests: comparison of the accuracy of some representative quantities for the HLL, Roe, and KT solvers. The columns report the global errors when convergence is reached. Regarding efficiency, the KT solver is typically 5%–10% slower than HLL, while Roe is typically a factor of 2 slower than HLL.

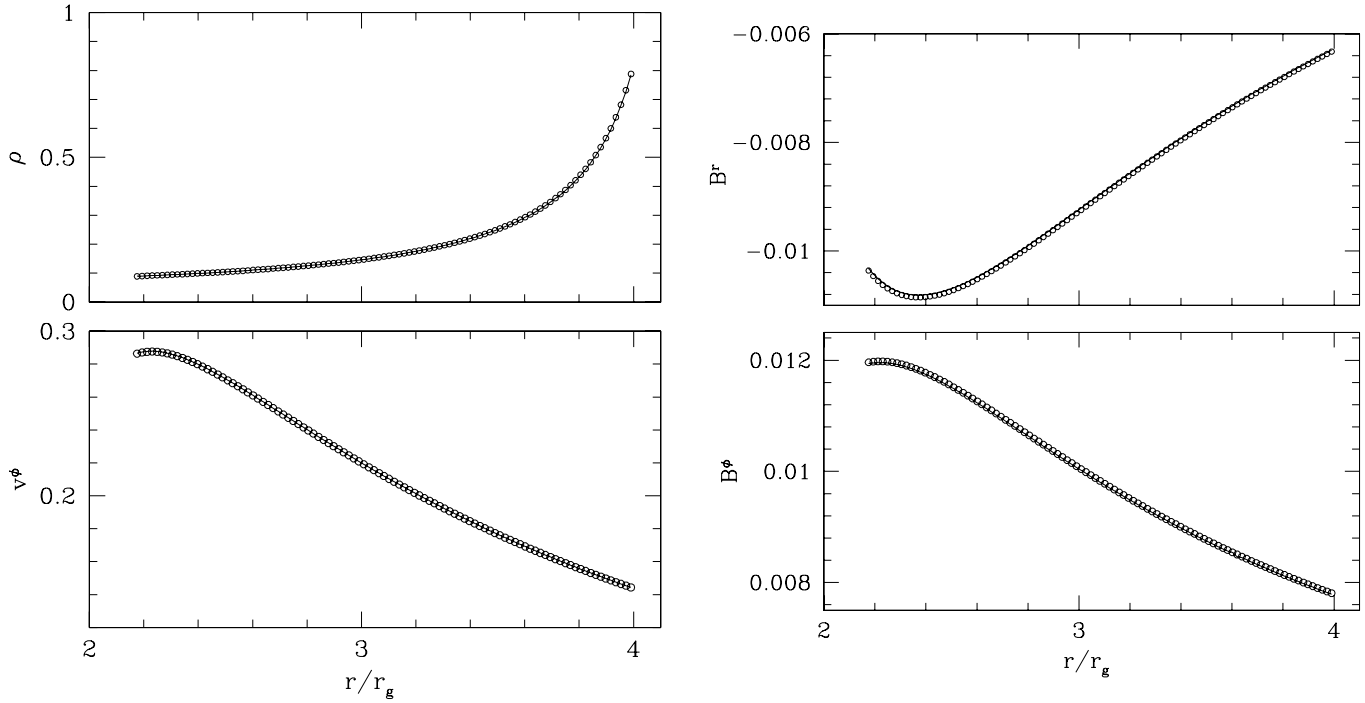

FIG. 4.—Comparison between the analytic solution (*solid line*) and the numerical converged solution obtained with the Roe-type Riemann solver (*circles*) for the magnetized accretion solution onto a Kerr black hole with spin parameter $a = 0.5$. The left panels report the rest-mass density ρ and the azimuthal velocity v^{ϕ}, while the right panels report the radial and the azimuthal components of the magnetic field, B^r and B^{ϕ}, all of them in geometrized units.

It is worth stressing that the HLL scheme, at least in our implementation, turns out to be the most accurate in the computation of the magnetic field.

5.4. *Thick Accretion Disks around Black Holes*

An intrinsic two-dimensional test for the code is provided by the stationary solution of a thick disk (or torus) orbiting around a black hole, described by Fishbone & Moncrief (1976), Kozlowski et al. (1978), and more recently by Font & Daigne (2002). The resulting configuration consists of a perfect barotropic fluid in circular non-Keplerian motion around a Schwarzschild or Kerr black hole, with pressure gradients in the vertical direction accounting for the disk thickness. These thick disks may possess a cusp on the equatorial plane through which matter can accrete onto the black hole.

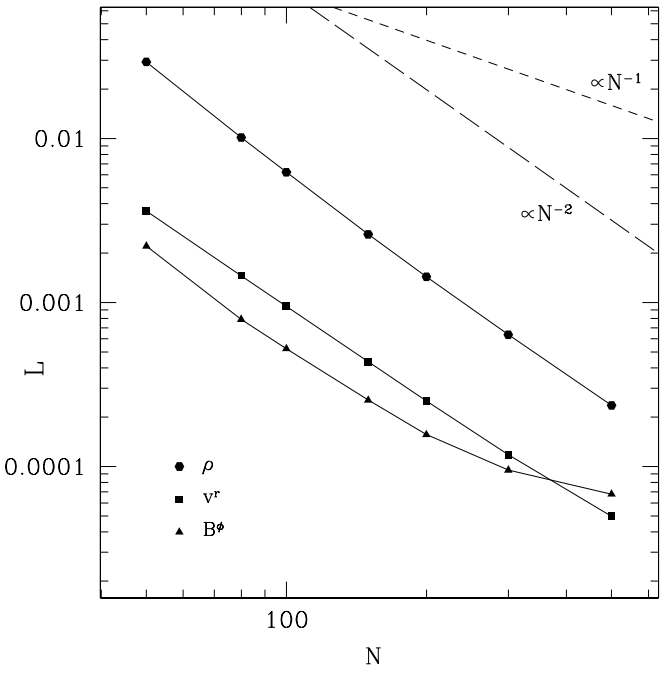

FIG. 5.—Error L of the rest-mass density, the radial velocity, and the toroidal magnetic field for the magnetized equatorial accretion in the Kerr metric. The short-dashed and long-dashed lines indicate first and second order of global convergence, respectively.

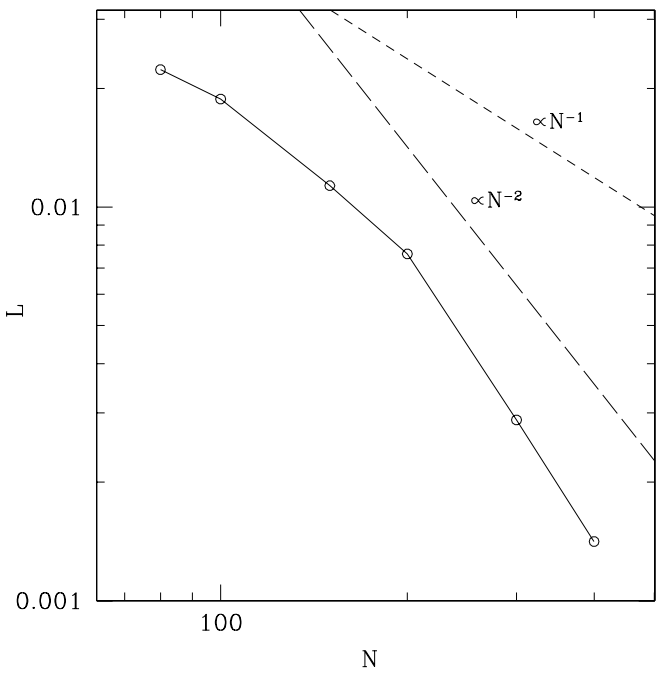

FIG. 6.—Unmagnetized thick accretion disk. The plot shows the error L of the rest-mass density when resolution is increased. The short-dashed and long-dashed lines indicate first and second order of global convergence, respectively.

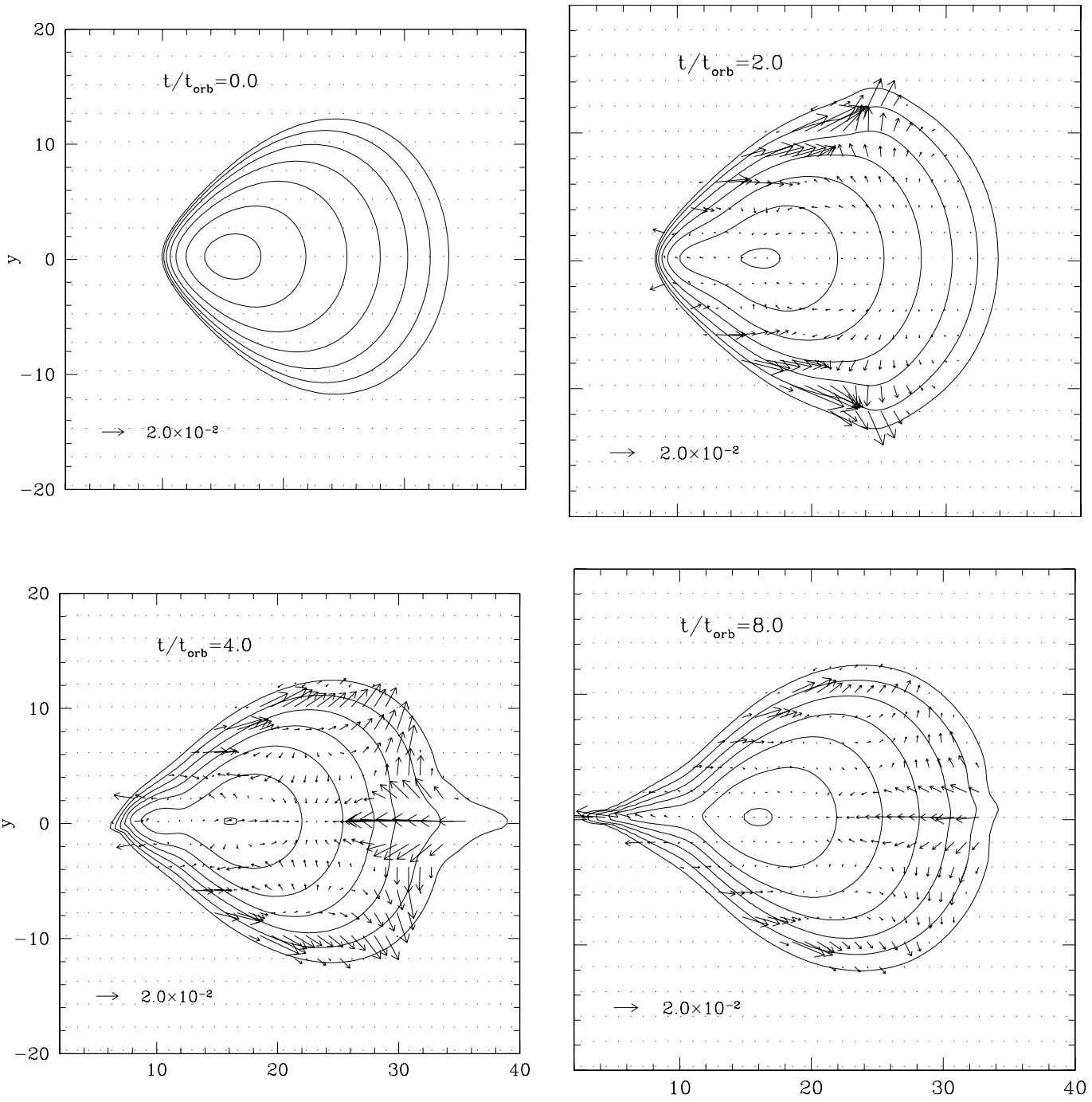

FIG. 7.—Velocity field and logarithmic isocontours of the rest-mass density. At four orbital periods an elongated high-density structure is formed near the equatorial plane, signaling the MRI in two-dimensional calculations.

In the following two subsections we describe our numerical tests for unmagnetized and magnetized thick disks, respectively. In both cases the effective potential at the inner edge of the disk is smaller than that at the cusp, thus providing initial conditions that are strictly stationary. For simplicity we limit our simulations to models with constant distribution of specific angular momentum $\ell = -u_\phi/u_t$, although the same qualitative results have been obtained with more general rotation laws.

5.4.1. *Unmagnetized Disk*

In testing the evolution of a purely hydrodynamical torus, we consider a model similar to the one used by De Villiers & Hawley (2003a) for the Schwarzschild metric, namely, a torus with specific angular momentum $\ell = 4.5$, position of the maximum density at $r_{\rm center} = 15.3$, and an effective potential at the inner edge such that the inner and outer radii on the equatorial plane are $r_{\rm in} = 9.34$ and $r_{\rm out} = 39.52$, respectively. We choose a polytropic EOS with $\gamma = 4/3$ and a polytropic constant K such that the torus-to-hole mass ratio is $M_t/M \sim 0.07$.

We have checked that the code can keep the stationarity of the initial equilibrium torus when evolved in time. Figure 6 shows the global order of convergence as computed from the rest-mass density ρ. The corresponding global error L reported in the figure, defined as $L \equiv \sum_{i,j=1}^{N} |\rho_{ij} - \rho_{a,ij}| / \sum_{i,j=1}^{N} \rho_{a,ij}$, is computed

after 10 orbital periods for each model, using a uniform numerical grid consisting of $N \times N$ grid points, whose specific values can be read off from the figure. As is apparent from Figure 6, the code reaches second order of convergence for reasonably high values of N (>200).

We note that in addition to the model just discussed we have also analyzed the performance of the code by comparing the evolution of additional hydrodynamical models that were studied by Font & Daigne (2002) and Zanotti et al. (2003) using independent codes based on HRSC schemes. In all the cases considered, corresponding to a number of different generalizations such as disks with power-law distributions of the specific angular momentum, disks in Kerr spacetime, and disks subject to the so-called runaway instability, the GRMHD code reproduced the same quantitative results of the independent hydrodynamical codes with differences less than 1%.

5.4.2. *Magnetized Disk*

As a final test we consider the evolution of a magnetized torus around a Schwarzschild black hole. In this case, however, a stationary solution that might provide self-consistent initial data for such magnetized disks is not available. Indeed, it can be proved (see Appendix B for a proof) that the hydrodynamical isoentropic type of models that we have used in the previous section for unmagnetized disks cannot be "dressed" with a magnetic field, to produce a force-free magnetized torus that satisfies the whole set of Maxwell's equations. Therefore, we follow the same pragmatic approach adopted by De Villiers & Hawley (2003a) and Gammie et al. (2003) and simply add an ad hoc poloidal magnetic field to the hydrodynamical thick-disk model. The magnetic field is generated by a vector potential $A_\phi \propto \max(\rho/\rho_c - C,\ 0)$, where ρ_c is the maximum rest-mass density of the torus and C is a free parameter that determines the confinement of the field inside the torus. The hydrodynamical torus is the same as the one considered in § 5.4.1, but endowed with a magnetic field characterized by a confinement parameter $C = 0.5$ and such that the average ratio of magnetic to gas pressure inside the torus is $\beta = 1.5 \times 10^{-3}$.

The four panels of Figure 7 display isocontours of the rest-mass density, logarithmically spaced, during the first few orbital periods of the evolution. These results correspond to a simulation employing the HLL solver with a computational grid of 200 radial zones and 100 angular zones. It was first shown by Balbus & Hawley (1991) that the dynamics of such magnetized thick disks is governed by the so-called MRI, which generates turbulence in the disk and helps explain the transport of angular momentum outward. In axisymmetry the development of the MRI is much less significant than in full three dimensions and manifests itself through the appearance of the so-called channel solution (De Villiers & Hawley 2003b). This feature of the solution becomes visible in our simulation after about three orbital periods, as shown in Figure 7, in the form of a high-density elongated structure near the equatorial plane. We report in Figure 8 two additional distinctive features that can be unambiguously attributed to the MRI. The first one, shown in the top panel, represents the transport of angular momentum (initially constant) outward, which acquires a Keplerian profile (indicated by a thick solid line) as the evolution proceeds. Correspondingly, the bottom panel shows the rapid increase of the (mean) magnetic pressure (*dashed line*) with respect to the gas pressure (*solid line*) during the first two orbital periods and due to the MRI-driven turbulence.

We note, however, that the present status of the numerical code does not allow us to evolve efficiently additional simulations with higher resolutions and with increasingly larger values of the magnetization parameter. As a result, the typical distortion of the isodensity contours produced by the MRI is not visible in Figure 7. A parallel version of the code is currently under development. This will allow for higher resolution simulations of magnetized disks in astrophysical contexts.

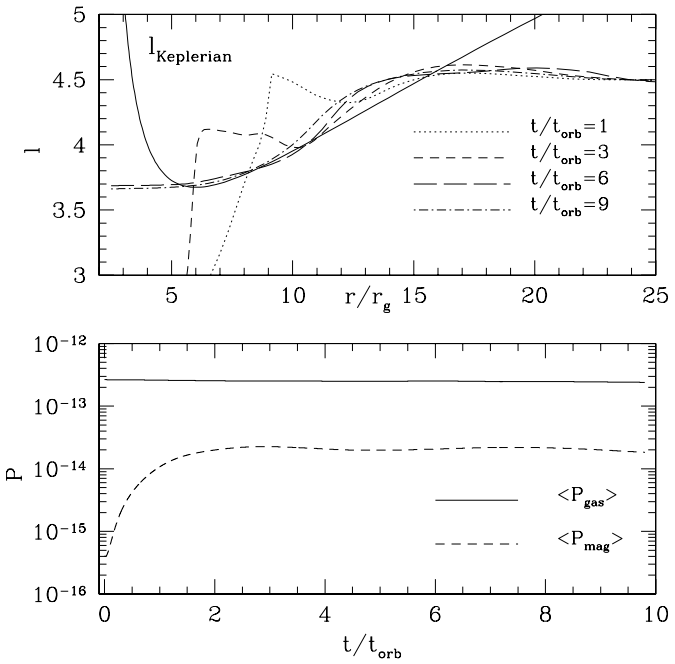

FIG. 8.—*Top*: Equatorial angular momentum approaches the Keplerian profile as an effect of the MRI. *Bottom*: Time evolution of the total gas pressure (*solid line*) and of the magnetic pressure (*dashed line*).

6. CONCLUSIONS

In this paper we have presented a procedure to solve numerically the GRMHD equations within the framework of the 3+1 formalism. The work reported here represents the extension of our previous investigation (Banyuls et al. 1997) where magnetic fields were not considered. The GRMHD equations have been explicitly written in conservation form to exploit their hyperbolic character in the solution procedure using Riemann solvers. Most of the theoretical ingredients that are necessary in order to build up HRSC schemes based on the solution of local Riemann problems have been discussed. In particular, we have described and implemented three alternative HRSC schemes, either upwind as HLL and Roe, or symmetric as KT. Our implementation of the Roe-type Riemann solver has made use of the equivalence principle of general relativity, which allows us to use, locally, the characteristic information of the system of equations in the special relativistic limit, following a slight modification of the procedure first presented in Pons et al. (1998). Further information regarding the renormalization of the eigenvectors of the GRMHD flux vector Jacobians has been deferred to an accompanying paper (L. Antón et al. 2006, in preparation). The work reported in this paper, hence, follows the recent stir of activity in the ongoing efforts of developing robust numerical codes for the GRMHD system of equations, as exemplified by the investigations presented in the last few years by a number of groups (De Villiers & Hawley 2003a; Gammie et al. 2003; Duez et al. 2005; Komissarov 2005).

Our formulation of the equations and numerical procedure has been assessed by performing the various test simulations discussed

in earlier works in the literature, including magnetized shock tubes in flat spacetimes, spherical accretion onto a Schwarzschild black hole, equatorial magnetized accretion in the Kerr spacetime, and evolution of thick accretion disks subject to the development of the MRI. The code has proved to be second-order accurate and has successfully passed all considered tests. In the near future we plan to apply this code in a number of astrophysical scenarios involving compact objects where both strong gravitational fields and magnetic fields need to be taken into account.

This research has been supported by the Spanish Ministerio de Educación y Ciencia (grants AYA2004-08067-C03-01, AYA2004-08067-C03-02, and SB2002-0128) and the Generalitat Valenciana (grant GV2005/244). The computations were performed on the Beowulf Cluster for Numerical Relativity *"Albert100"* at the University of Parma and on the SGI/Altix3000 computer *"CERCA"* at the Servicio de Informática de la Universidad de Valencia. O. Z. is grateful to Luciano Rezzolla for carefully reading the paper.

APPENDIX A

MAGNETIZED MICHEL ACCRETION

In this appendix we prove that the only consistent solution for a force-free magnetic field added to the spherically symmetric accretion of a perfect fluid onto a Schwarzschild black hole fulfills the condition $\mathcal{J} = 0$. To prove this result, we start from the fact that the form of the four-current compatible with a force-free magnetic field is given by (Oron 2002)

$$\mathcal{J}^{\mu} = \rho_q u^{\mu} + \eta b^{\mu}, \tag{A1}$$

where ρ_q is the proper charge density. If we write explicitly the four vanishing components of the electric field in the comoving frame of the accreting fluid, $F_{\mu\nu}u^{\nu} = 0$, recalling that the velocity field is given by $u^{\mu} = (u^0,\ u^1,\ u^2,\ u^3) = (u^t,\ u^r,\ 0,\ 0)$, we find

$$F_{01} = 0, \tag{A2}$$

$$F_{02}u^0 + F_{12}u^1 = 0, \tag{A3}$$

$$F_{31} = 0, \tag{A4}$$

where we have also used the fact that $F_{03} = \partial_0 A_3 - \partial_3 A_0 = 0$. Let us next consider the first couple of Maxwell equations

$$F_{[\alpha\beta,\gamma]} = 0, \tag{A5}$$

where the comma denotes partial differentiation. After writing them explicitly for all possible combinations, we obtain

$$F_{01,2} + F_{12,0} + F_{20,1} = 0, \tag{A6}$$

$$F_{01,3} + F_{13,0} + F_{30,1} = 0, \tag{A7}$$

$$F_{02,3} + F_{23,0} + F_{30,2} = 0, \tag{A8}$$

$$F_{12,3} + F_{23,1} + F_{31,2} = 0. \tag{A9}$$

By the symmetries of the spacetime and by equations (A2)–(A4), this system reduces to

$$F_{02,1} = 0, \tag{A10}$$

$$F_{23,1} = 0. \tag{A11}$$

Summarizing, among the six components of the antisymmetric electromagnetic tensor $F_{\mu\nu}$, three of them vanish, namely, $F_{01} = F_{03} = F_{13} = 0$. Among the remaining three, only two are independent, since the constraint given by equation (A3) has to be fulfilled. Furthermore, according to equations (A10) and (A11), F_{02} and F_{23} are functions of the angle θ only, $F_{02} = F_{02}(\theta)$ and $F_{23} = F_{23}(\theta)$, and are therefore constants along fluid lines. Taking all this into account, we can write the components of the magnetic field explicitly, using the definition given by equation (11) in the main text,

$$b^0 = \frac{1}{\sqrt{-g}} F_{23} u_1, \tag{A12}$$

$$b^1 = -\frac{1}{\sqrt{-g}} F_{23} u_0 = -\frac{b^0 u_0}{u_1}, \tag{A13}$$

$$b^2 = 0, \tag{A14}$$

$$b^3 = \frac{1}{\sqrt{-g}} (F_{02} u_1 - F_{12} u_0) = -\frac{F_{02}}{\sqrt{-g} u^1}. \tag{A15}$$

Note that equation (A13) can be alternatively computed from the condition $b^{\mu}u_{\mu} = 0$.

Up to this point we have shown that the magnetic field is completely determined by two constants, F_{23} and F_{02}. We now consider the second couple of Maxwell equations, namely, $\nabla_\nu F^{\mu\nu} = 4\pi\mathcal{J}^\mu$. According to the assumption on the four-current, equation (A1), and on the four-velocity in the case of spherical accretion, these equations become

$$\partial_2\left(\sqrt{-g}F^{02}\right) = 4\pi\sqrt{-g}\left(\rho_q u^0 + \eta b^0\right), \tag{A16}$$

$$\partial_2\left(\sqrt{-g}F^{12}\right) = 4\pi\sqrt{-g}\left(\rho_q u^1 + \eta b^1\right), \tag{A17}$$

$$\partial_1\left(\sqrt{-g}F^{21}\right) = 0, \tag{A18}$$

$$\partial_2\left(\sqrt{-g}F^{32}\right) = 4\pi\sqrt{-g}\eta b^3, \tag{A19}$$

where $F^{02} = F_{02}/g_{00}g_{22}$ and $F^{12} = F_{12}/g_{11}g_{22}$. From equation (A18) it follows that the term F_{12}/g_{11} must be a function of the angular coordinate θ only, which, recalling equation (A3) and the fact that both u^0 and u^1 are functions of r, implies that $F_{12} = F_{02} = 0$. As a result, the toroidal component of the magnetic field b^3 vanishes. Moreover, according to equation (A19), the term $F_{23}/(r^2\sin\theta)$ must be a function of r only. Given that $F_{23} = F_{23}(\theta)$, it must be $F_{23} = A\sin\theta$, with A a constant. Finally, equations (A16) and (A17) are now reduced to the following homogeneous system in the unknowns ρ_q and η:

$$u^0\rho_q + b^0\eta = 0, \tag{A20}$$

$$u^1\rho_q + b^1\eta = 0. \tag{A21}$$

From the orthogonality condition $b^\mu u_\mu = 0$ and the normalization condition $u^\mu u_\mu = -1$, we obtain that the determinant of the homogeneous system, $u^0 b^1 - u^1 b^0$, is nonzero, and therefore the only possible solution is the trivial one, $\rho_q = 0$ and $\eta = 0$, which according to equation (A1) leads to $\mathcal{J} = 0$. This concludes the proof.

APPENDIX B

MAGNETIZED THICK ACCRETION DISK

In this appendix we show that it is not possible to build a consistent stationary and axisymmetric solution for a magnetized torus by simply adding a force-free magnetic field to the hydrodynamic equilibrium model of an isoentropic thick accretion disk (Kozlowski et al. 1978; Font & Daigne 2002). The proof, which for simplicity we limit to the case of Schwarzschild spacetime but can be extended to a Kerr black hole as well, could follow the same reasoning of the previous appendix. However, the demonstration is more direct if one exploits some topological properties of the expected solution. In fact, from Maxwell equations it is possible to show that the magnetic field of a perfectly conducting medium endowed with a purely toroidal motion has to be purely poloidal, i.e., $b^r \neq 0$, $b^\theta \neq 0$, while $b^t = b^\phi = 0$. Under these conditions, the magnetic field lines lie on the surfaces of constant magnetic potential A_ϕ (magnetic surfaces), which coincide with the surfaces of constant angular velocity $\Omega = u^\phi/u^t$. This property prevents the generation of a toroidal component of the magnetic field, even in the presence of differential rotation (Ferraro's theorem), and allows us to introduce a new coordinate system (x_1, x_2) such that x_1 varies along the poloidal field lines and x_2 is constant along them (Oron 2002). In this new coordinate system the magnetic field will only have one nonvanishing component b^1, while $b^2 = 0$.

According to Bekenstein & Oron (1979), for a force-free magnetic field in an isoentropic flow the quantity $U = u^t u_\phi$ is constant along the magnetic surfaces, and it can be used to define the new coordinate x_2. In the case of circular motion in Schwarzschild spacetime this quantity reads

$$U = -\frac{\Omega g_{\phi\phi}}{g_{tt}(1-\Omega\ell)}, \tag{B1}$$

where $\ell = -u_\phi/u_t$ is the specific angular momentum. According to von Zeipel's theorem (von Zeipel 1924), ℓ is constant along surfaces of constant Ω for the class of barotropic hydrodynamic models that we are considering. Therefore, both Ω and ℓ are constant along magnetic surfaces and the new coordinate x_2 can be defined as

$$x_2 = \left[\frac{U}{\Omega}(1-\Omega\ell)\right]^{1/2} = \left(-\frac{g_{\phi\phi}}{g_{tt}}\right)^{1/2} = \frac{r\sin\theta}{(1-2M/r)^{1/2}}, \tag{B2}$$

which is the so-called von Zeipel parameter (Chakrabarti 1985). The other coordinate x_1 can be chosen such that orthogonality between x_1 and x_2 is preserved, i.e., $g_{12} = 0$. After some calculations involving straightforward metric coefficient transformations, this choice yields

$$x_1 = (r-3M)\cos\theta. \tag{B3}$$

In computing equation (B3) we have made the reasonable *Ansatz* that x_1 is factorized as $x_1 = p(r)q(\theta)$. Oron (2002) has shown that, in order to satisfy the second couple of Maxwell's equations and the scalar equation $\nabla_\mu(hb^\mu) = 0$, which can be proved to hold for any isoentropic magnetized flow, the following factorization in terms of generic functions of x_1 and x_2 must exist:

$$\frac{g_{11}}{g_{22}\Delta(u^t)^4} = f(x_1)h(x_2), \tag{B4}$$

where $\Delta = -g_{tt}g_{\phi\phi}$ in the Schwarzschild metric. From the normalization condition $u^\mu u_\mu = -1$ it follows that $(u^t)^2 = 1/[g_{tt}(1 - x_2^2\Omega^2)]$, and equation (B4) becomes

$$\left(1 - \frac{2M}{r}\right)^2 (x_2)^2 \left[1 - \Omega^2 (x_2)^2\right]^{-2} = f(x_1)h(x_2). \tag{B5}$$

Since $\Omega = \Omega(x_2)$, equation (B5) requires that the term $1 - 2M/r$ is factorizable as $f(x_1)h(x_2)$, which can be shown not to be possible. Hence, the constraint given by equation (B4) cannot be met, and a force-free magnetized torus built from the isoentropic hydrodynamic model of a thick accretion disk cannot be obtained.

REFERENCES

Anile, A. M. 1989, Relativistic Fluids and Magneto-Fluids (Cambridge: Cambridge Univ. Press)
Arnowitt, R., Deser, S., & Misner, C. W. 1962, in The Dynamics of General Relativity, ed. L. Witten (New York: Wiley), 227
Balbus, S. A., & Hawley, J. F. 1991, ApJ, 376, 214
Balsara, D. 2001, ApJS, 132, 83
Banyuls, F., Font, J. A., Ibáñez, J. M., Martí, J. M., & Miralles, J. A. 1997, ApJ, 476, 221
Baumgarte, T. W., & Shapiro, S. L. 2003, ApJ, 585, 921
Bekenstein, J. D., & Oron, E. 1979, Phys. Rev. D, 19, 2827
Blandford, R. D., & Payne, D. G. 1982, MNRAS, 199, 883
Blandford, R. D., & Znajek, R. L. 1977, MNRAS, 179, 433
Bocquet, M., Bonazzola, S., Gourgoulhon, E., & Novak, J. 1995, A&A, 301, 757
Brio, M., & Wu, C. C. 1988, J. Comput. Phys., 75, 400
Chakrabarti, S. K. 1985, ApJ, 288, 1
Del Zanna, L., Bucciantini, N., & Londrillo, P. 2003, A&A, 400, 397
De Villiers, J., & Hawley, J. F. 2003a, ApJ, 589, 458
———. 2003b, ApJ, 592, 1060
Duez, M. D., Liu, Y. T., Shapiro, S. L., & Stephens, B. C. 2005, Phys. Rev. D, 72, 024028
Evans, C., & Hawley, J. F. 1988, ApJ, 332, 659
Fishbone, L. G., & Moncrief, V. 1976, ApJ, 207, 962
Font, J. A. 2003, Living Rev. Relativity, 6, 4
Font, J. A., & Daigne, F. 2002, MNRAS, 334, 383
Font, J. A., Ibáñez, J. M., Marquina, A., & Martí, J. M. 1994, A&A, 282, 304
Font, J. A., Miller, M., Suen, W., & Tobias, M. 2000, Phys. Rev. D, 61, 044011
Gammie, C. F. 1999, ApJ, 522, L57
Gammie, C. F., McKinney, J. C., & Tóth, G. 2003, ApJ, 589, 444
Gardiner, T. A., & Stone, J. M. 2005, J. Comput. Phys., 205, 509
Giacomazzo, B., & Rezzolla, L. 2005, J. Fluid Mech., submitted
Harten, A., Lax, P. D., & van Leer, B. 1983, SIAM Rev., 25, 35
Ibáñez, J. M., Aloy, M. A., Font, J. A., Martí, J. M., Miralles, J. A., & Pons, J. A. 2001, in Godunov Methods: Theory and Applications, ed. E. F. Toro (New York: Kluwer), 485
Koide, S. 2003, Phys. Rev. D, 67, 104010
Koide, S., Meier, D. L., Shibata, K., & Kudoh, T. 2000, ApJ, 536, 668
Koide, S., Shibata, K., & Kudoh, T. 1998, ApJ, 495, L63
Koide, S., Shibata, K., Kudoh, T., & Meier, D. L. 2002, Science, 295, 1688
Koldoba, A. V., Kuznetsov, O. A., & Ustyugova, G. V. 2002, MNRAS, 333, 932
Komissarov, S. S. 1999, MNRAS, 303, 343
Komissarov, S. S. 2005, MNRAS, 359, 801
Kouveliotou, C., et al. 1998, Nature, 393, 235
Kozlowski, M., Jaroszynski, M., & Abramowicz, M. A. 1978, A&A, 63, 209
Kurganov, A., & Tadmor, E. 2000, J. Comput. Phys., 160, 241
Leismann, T., Antón, L., Aloy, M. A., Müller, E., Martí, J. M., Miralles, J. A., & Ibáñez, J. M. 2005, A&A, 436, 503
LeVeque, R. J. 1998, in Computational Methods for Astrophysical Fluid Flow, ed. O. Steiner & A. Gautschy (Berlin: Springer), 1
Londrillo, P., & del Zanna, L. 2004, J. Comput. Phys., 195, 17
Lucas-Serrano, A., Font, J. A., Ibáñez, J. M., & Martí, J. M. 2004, A&A, 428, 703
Martí, J. M., & Müller, E. 2003, Living Rev. Relativity, 6, 7
McKinney, J. C., & Gammie, C. F. 2004, ApJ, 611, 977
Michel, F. 1972, Ap&SS, 15, 153
Oron, A. 2002, Phys. Rev. D, 66, 023006
Papadopoulos, P., & Font, J. A. 2000, Phys. Rev. D, 61, 024015
Penrose, R. 1969, Nuovo Cimento, 1, 252
Pons, J. A., Font, J. A., Ibáñez, J. M., Martí, J. M., & Miralles, J. A. 1998, A&A, 339, 638
Romero, R., Martí, J. M., Pons, J. A., Miralles, J. A., & Ibáñez, J. M. 2005, J. Fluid Mech., 544, 323
Ryu, D., Jones, T. W., & Frank, A. 1995, ApJ, 452, 785
Ryu, D., Miniati, F., Jones, T. W., & Frank, A. 1998, ApJ, 509, 244
Shibata, M., & Font, J. A. 2005, Phys. Rev. D, 72, 047501
Shibata, M., & Sekiguchi, Y. 2005, Phys. Rev. D, 72, 044014
Shu, C., & Osher, S. 1988, J. Comput. Phys., 77, 439
Sloan, J., & Smarr, L. L. 1985, in General Relativistic Magnetohydrodynamics, ed. J. L. J. Centrella & R. Bowers (Boston: Jones & Bartlett), 52
Takahashi, M., Nitta, S., Tatematsu, Y., & Tomimatsu, A. 1990, ApJ, 363, 206
Toro, E. F. 1997, Riemann Solvers and Numerical Methods for Fluid Dynamics (Berlin: Springer)
Tóth, G. 2000, J. Comput. Phys., 161, 605
van Putten, M. H. P. M. 1991, Commun. Math. Phys., 141, 63
———. 1993, J. Comput. Phys., 105, 339
von Zeipel, H. 1924, MNRAS, 84, 665
Wilson, J. R. 1979, in Sources of Gravitational Radiation, ed. L. Smarr (Cambridge: Cambridge Univ. Press), 423
Yokosawa, M. 1993, PASJ, 45, 207
———. 1995, PASJ, 47, 605
Yokosawa, M., & Inui, T. 2005, ApJ, 631, 1051
Zanotti, O., Rezzolla, L., & Font, J. A. 2003, MNRAS, 341, 832
Zhang, X. 1989, Phys. Rev. D, 39, 2933